U S

University of Stavanger

Faculty of Science and Technology

MASTER'S THESIS

Study program/ Specialization:	Spring semester, 2013
Industrial economics Project management	Open

Writer: Therese N. Nordbø	………………………………………… (Writer's signature)

Faculty supervisor: Thor-Martin Svartås	

Title of thesis:

Hydrate growth kinetics: A study on the relation between energy release rates and gas consumption rates during methane hydrate formation and growth.

Credits (ECTS): 30

Key words: Methane hydrates, growth	Pages: 94 + enclosure: 15 Stavanger, 17.06/2013 Date/year

I

Acknowledgement

My master was initiated in autumn 2012. As I really enjoy student lifestyle. It was with a mixture of relief, joy and despair I embarked upon my next study. To be fed with new information day by day, to notice that I grew from it, yet have freedom gives me a great feeling. Five years, which is over 1/6 of my life, has been spent at the University of Stavanger, so I think it's time to take the plunge into working life. Although it's new and a little scary, I believe I'm ready with all the background knowledge I have aquired. However, before I can do this, I personally feel there is something essential missing, there remains a qualification that I have to have, one last mission, the hallmark of the Master- The Master thesis.

I sat down and thought over recent years. I reflected upon what I remembered and what I liked best. The Bachelor thesis stands out the most. I got a feeling of mastery when I was writing it, I learned a lot and also had fun. Although I had a steep learning curve when I wrote the thesis about gas hydrates, I also found that I had so much more to learn about this subject. There is so much uncertainty around it, so I decided to seek out Thor Martin Svartås and ask if it was possible to also write a master thesis for him. As always, he was positive and said yes.

So therefore, I will first and foremost give a large thank you to Mr. Thor Martin Svartås for the great help. Everyday he has been available, given positive and especially helpful guidance. He has enthusiastically encouraged me throughout my research. He told me that my study was just like a toolbox, and the subjects are different types of tools, which together makes an entirety. I feel that my toolbox is now well enough equipped for me to take the plunge into employment, so again, thank you Thor Martin.

I would also like to thank PhD student Remi Ermpagano Meindinyo and Professor Runar Bø. We have worked together closely this season and found useful information. I am also very grateful for the support received from Svein Myrhen and Sivert Bakken Drangeid. They scurried around and fixed computer and other equipment problems that appeared and challenged us. Thank you both.

Last but not least, I wish to thank the rest of the crew I worked along side during the last six months in the hydrate lab. It would not have been so fun without them. Good luck with the last two years of your studies, and enjoy the good life as a student!

Abbreviations

- An easier way to find the explanation of the abbreviations

AA   Anti agglomerants

AUC   Area under curve

CF   Conversion factor

DW   Distilled water

g   Gas

HC   Hydrocarbon

HEN   Heterogeneous nucleation

HON   Homogeneous nucleation

KGraph   KaleidaGraph

KHI   Kinetic Hydrate Inhibitors

LDHI   Low Dose Hydrate Inhibitors

sI   Structure I

sII   Structure II

sH   Structure H

THI   Thermodynamic Hydrate Inhibitors

VS.   Versus

w   Water

Symbols

a	Is a constant
A_0	The outer wall surface
$A_{(g-1)}$	Gas-liquid interface area
A_p	The surface area of each particle
b	Is the flow rate
C_I	Transfer coefficient
c_p	Heat capacity at constant pressure
$c_{p,g}$	Gas heat capacity
c_w	Heat capacity water
c_{wo}	Initial concentration of water
$(dn_i/dt)_p$	Number of gas moles consumed per section by the hydrate
f_i^b	Fugacity of component i in the bulk liquid
f_i^{eq}	Equilibrium fugacity of component i in the liquid at the hydrate interface
$(f_i^b - f_i^{eq})$	Defines the overall driving force
f_w	Fractional water conversion into hydrates
h	Hours
h_i	Inner thermal coefficient
h_o	Outher thermal coefficient
H_{pro}	Formation enthalpy of products
H_{reac}	Formation enthalpy of reactants
K*	Hydrate formation growth rate constant, representing a combined rat necessary for constant diffusion (mass transfer) and adsorption (reaction) processes
k_r	Reaction rate constant
k_d	Mass transfer coefficient through the film around the particle
m_w	Mass of water
n	Number of moles
$n_{g,consumed}$	The total amount of gas consumed at a given stage of the process
$n_{w,consumed}$	The total amount of water consumed at a given stage of the process
$n_{w,init}$	The initial amount of water
N_g	Mole of gas
P	Pressure
$\dot{q}_R$	The heat of reaction
$\dot{Q}_{g,m}$	The measured volumetric gas flow at time step m
r	Radius
r_c	Critical radius
R	Universal gas constant (the real gas equation)
RPM	Revolutions per minute
Sm3	Standard cubic meter
T	Temperature
T_{eq}	Equilibrium temperature

$(T_I - T_0)$	The temperature difference across the wall
t_{int}	The duration of the time interval for the average
T_I^P	The start iside cell temperature
T_I^{P+1}	The current inside cell temperature
TI_r	Representative internal temperature
T_g	Temperature gas phase
T_O	Cooling water temperature (outher temperature)
T_O^{p+1}	The current outer temperature
T_w	Temperature water phase
V	Volume
W	Work
Wt.%	Weight percentage/mass percent
X_I	An unknown temperature
x_{int}	Bulk liquid mole fraction of the component
Z	Compressibility factor
Å	Unit (1 Å = 1 × 10^{-10} meter)
ϒ	Surface tension [dyn/cm] (1 dyn/cm = 10-3 N/m)
ΔG	Gibbs free energy
ΔG_{crit}	Maximum value to ΔG
ΔG_s	Surface excess free energy
ΔG_v	Volume excess free energy
Δg_v	Free energy change per volume
Δh_H	Heat of hydrate formation per unit mass of hydrate
ΔH	Enthalpy
ΔS	Entropy
ΔT	During Cooling
Δ μ	Over Saturation
θ	Angle of contact between hydrate crystal and surface
σ	Surface tension between the liquid crystal
ф	Fractional used to go from ΔG_{crit} in homogeneous nucleation to $\Delta G'_{crit}$ in heterogeneous nucleation
δ	Hydrate film thickness
λ_h	The thermal conductivity of hydrate
λ_w	The thermal conductivity of water
$\frac{\partial T}{\partial t}\Big|_I$	The inner temperature gradients
$\frac{\partial t}{\partial x}\Big|_{X=x_h-}$	The hydrate-side temperature gradients where x = x_h
$\frac{\partial t}{\partial x}\Big|_{X=x_h+}$	The water-side temperature gradients where x = x_h

Abstract

The relation between mass transfer, energy transfer and growth rates has been examined during methane hydrate formation in stirred cell reactors. This was done to improve understanding rate determining factors during hydrate formation and growth.

In stirred cell reactor heat transfer and heat transfer rates will be functions of stirring rate and through boundary layers at the wall. The heat transfer rate is also function of temperature gradients. Experiments have thus been conducted at three different stirring rates and temperatures levels to evaluate the effect of stirring and temperature gradients on heat transfer.

Experiments have been conducted using two different cell setups, a smaller cell having a volume of 141.4 ml and with inner diameter of 60 mm, outer diameter of 90 mm and a height of 50 mm, and a larger cell having a volume of 318.1 ml and with an inner diameter of 90 mm, outer diameter of 120 mm and a height of 50 mm. The cell systems were connected to a high pressure methane reservoir via a pressure reduction valve and a flow meter and operated in an open mode to maintain constant pressure throughout the experiments.

In the smaller cell hydrate formation and growth was studied at three different experimental temperatures of 6, 7 and 8 °C and at stirring rates of 500, 700 and 1200 rpm using either 50 ml or 100 ml distilled water (DW). In the larger cell experiments were conducted at 8 °C and 700 rpm to examine effects of cell size and radial heat flow. The volume of water was either 112.5 ml or 225 ml for the large cell experiments.

Hydrate growth rates were estimated analyzing the amount of gas passing through the flow-meter per time unit and the amount of heat released (exothermic reaction) through temperature measurements. The analysis was terminated when heat release was observed to decay and prior to complete conversion of water into hydrates to reduce effects of increasing hydrate mass on heat transfer. The growth rate was initially relatively fast and decaying towards the end of the period analyzed. The analyzed growth period could be devided into three different rate section (Initial rate 1, Mid-section rate 2 and End-section rate 3) and within each section the rate could be approximated a linear function of time.

Gas consumption by hydrate formation was used to calculate the heat production and heat flow into the cell. Heat flow out of the cell reactor was calculated on basis of measured temperature differences and the required heat input to balance the heat loss was estimated by simulations. Ideally this estimated heat input should be equal with the energy released by hydrate formation as calculated from the measured gas consumption during the process. The analysis was terminated when heat release was observed to decay as function of time and prior to complete conversion of water into hydrates to reduce effects of increasing hydrate mass on heat transfer.

Discrepancies between energy / heat flow into the cell calculated from formation enthalpy and a value estimated on the basis of temperature measurements was used to evaluate the effect of stirring rate on heat transfer and the used heat transfer coefficients during simulations.

Generally the simulated heat flow into the cell was higher than that calculated from the formation enthalpy indicating that heat transfer coefficients were overestimated.

Table of contents

List of figures

List of tables

1. INTRODUCTION

1.1 Background Knowledge

Gas hydrates are non-stoichiometric, crystalline substances formed by water and non-polar, smaller gas molecules. In the hydrate gas molecules, are entrapped in a lattice formed by water through hydrogen bonds. The lattice is composed of cavities of various sizes that house the gas molecules and the gas molecules are bound in the lattice through weak van der Waals forces. The water is called host molecules while the gas molecules are called guests. Gas hydrates are formed naturally or artificially in the environment where pressure is high and the temperature is low, and where free water is in contact with hydrocarbon gases.

The existence of natural gas hydrates was first identified by Davy in 1810 through formation of chlorine hydrate in the laboratory (Davy, 1811). Gas hydrates remained as curiosity of only academic interest until Hammerscmidt discovered that gas hydrates was the cause of gas transmission pipeline blockage in 1934 (Hammerschmidt, 1934). Since then the importance of gas hydrates as nuisance for the oil and gas production industry resulted in increased research interest on gas hydrate formation and prevention. Two different hydrate structures were identified and described by von Stackelberg through X-ray diffraction analysis (Stackelberg, 1954 and 1956) and in 1987 a third structure was identified by Ripmeester and his group through NMR analysis (Ripmeester et al. 1987).

The first decades after Hammerschmidts identification of gas hydrates as a problem during oil and gas production, the research on hydrates were focused on thermodynamics of formation and prevention to enable the industry to foresee the conditions at which hydrates may form and to take the needed precautions adding thermodynamic hydrate inhibitors (THI, antifreezes). In 1965 Makogon reported the existence of gas hydrates in permafrost regions and since then research on natural gas hydrates as potential future energy source was initiated. Kvenvolden and his group have presented several papers on geology and natural gas hydrates in sediments and permafrost (Kvenvolden and McMenamin, 1980, Kvenvolden et al, 1993) and in 1989 he reported gas hydrates at the Vøringe Platået outside middle of Norway (Kvenvolden et al, 1989).

Up to the end of 1980's beginning of 1990's hydrate prevention by use of large amounts thermodynamic inhibitors was most commonly method used. From end 1980's and up til now development of low dosage hydrate inhibitors (LDHI) have been focused and the history of LDHI development has lately been reviewed by M.A. Kelland (Kelland, 2006).

Even though a lot of research has been done on gas hydrates during the later years, the mechanisms by which they form and how and where they develop and grow to plugs in pipelines are not completely understood. As the exploration, discovery and development of new fields are moved towards deeper waters and colder region better methods to handle hydrate problems has to follow to make productions from such fields economic feasible. Hydrate formation is exothermic process and heat is released during formation leading to temperature increase in the region close to the site of formation. Most models on the kinetics of hydrate formation and growth are based on mass transfer while heat transfer is regarded the limiting factor during dissociation. (Sloan and Koh, 2008) The importance of heat transfer could be underestimated and monitoring temperature changes / temperature fluctuations in a pipeline might give early warning and potentially enable precautions to be taken before hydrates block the line.

1.2 Definition of the thesis

This thesis is based on examining the relationship between hydrate growth (measured by gas consumption via flow measurements), temperature development and energy production in a cell reactor during hydrate formation and growth. This could be done through measurements of the temperature development in the cell balanced against simulated heat flow out of the system and into the cooling water during the growth process. Correlations between growth rates calculated via gas consumption rates and energy flow in the system could then be used to analyse changes in heat transfer properties and boundary layers due to increasing amount of hydrate in the system. The aim of this master thesis is to investigate whether a model based on energy flows in the system (heat transfer model) can describe the growth kinetics as well as a model based on mass flow gas into the system (mass transfer model).

The method used estimation of the energy output of the system / quantified on the basis of gas consumption rates (measured) and the enthalpy of formation of the hydrate and temperature development (measured) as a function of energy production and energy loss from the system (simulated). The present study is conducted on methane hydrate (one-component gas) where values for enthalpy of formation are well defined and known from the literature.

The focus on this master is on the energy flow in relation to the growth rate of hydrate in the system.

2 LITERATURE REVIEW

2.1 Gas hydrate structure

Gas hydrates are formed by water and small gas molecules that are assembled in various crystal structures. Their consistence can be compared to snow, ice and slush. The main difference between ice and hydrate is that the ice is formed from pure water, while the hydrate not can be formed without guest molecules.

Hydrates are classified according to the layout of the water molecules that is in the crystals, which means that they are classified according to the crystal structure. In the 1950's Stachelberg and colleagues (1954 and 1956) identified the cubic hydrate structures, sI and sII, through X-ray diffraction. In 1987, Ripmeester discovered a new structure, hexagonal structure H (sH). The structure that is formed depends on the gas composition, the pressure and the temperature, and which cavity is included in the structure (Ripmeester et al. 1987).

SI and sII consists of small and large cavities, while sH consists of small, medium and large cavities. Since the various structures have different sizes of cavities they accommodate different types of guest molecules in the three different structures. In order to determine an upper limit on how large a guest molecule can be in a given cavity; Davidson suggeste (1971) that one could draw Van der Waals radius (1.4 Å) from a water molecule from the average radius of the respective cavity. By calculating the ratio has been found that in order to form hydrate with a pure gas is lower ratio boundary around 0.76 and the upper limit about 1.0. Is the number less than 0.76, the guest molecule is too small to stabilize the cavity. If the number is greater than 1.0 molecule, it will not fit without stretching the cavity. So the structure is dependent on the size of the gas molecule forming the hydrate, and whether it is a pure gas or a gas mixture. (Sloan and Koh, 2008)

Lattice structure around the small cavities in the unit cell is geometrically similar for all the three hydrate structures. This means that they may house the same type of gas components (guests) not necessarily being responsible for the formation of the given structure. The large voids are of different size for each structure, and will hose the gas components being responsible for the formation of the given structure. 1 sm^3 hydrate can contain between 150-

180 sm^3 gas, which is a huge amount considering that there normally can be only one gas molecule in each cavity. These cavities can accommodate various gas molecules with size between 3-7 Å. An entire cavity need not be completely full of gas for it to be a stable hydrate, but that crystal devices should remain stable within certain temperature and pressure ranges, the gas molecules occupy a certain fraction of lattice structures. (Sloan and Koh, 2008)
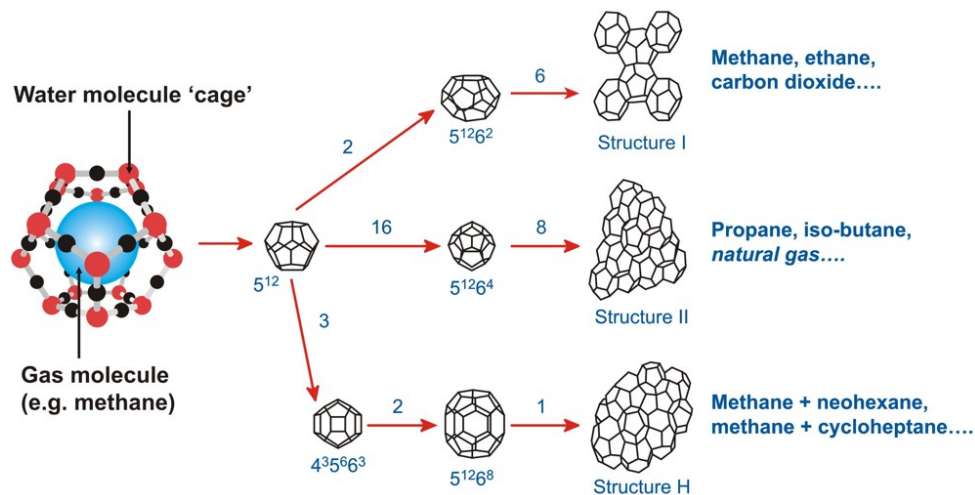
Figure 2.1: The three structures of gas hydrates (Heriot Watt University)

2.1.1 Structure I, SI

SI is the structure with the simplest hydrate structure, and has a cubical shape. It consists of two types of cavities, dodecahedron and tetrakaidecahedron. The dodecahedron is a 12-sided polyhedron where each face is a pentagon twelve edge 5^{12}, and is the smallest of the cavities. It contains 20 molecules of water with 30 hydrogen bonds, and has a radius of 3.95 Å. During a "normal" temperature and pressure may cavities contain CH_4, N_2, H_2S, H_2, Kr, Ar, and other non-polar gas molecules. Tetrakaidecahedron is a 14-sided polyhedron with 12 pentagonal and two hexagonal side faces, $5^{12} 6^2$. This large cavity containing 26 water molecules and has a radius of 4.33 Å. The cavities can contain including CO_2 and C_2H_6. Methane can occupy both the small and large cavities, while ethane can only occupy the large. (Sloan and Koh, 2008)

Together comprises the unit sI hydrate cell of 46 molecules of water arranged in lattice around 8 cavities. Of these eight cavities 2 of them are small and 6 of them large. (Sloan and Koh, 2008)

SI is formed only if the guest molecules are less than propane.

2.1.2 Structure II, sII

In contrast to the simple structure of the SI is SII much more complex, but still has a cubical shape. SII has the same concept, consisting of small and large cavities. The dodecahedron has exactly the same shape as that of SI, a 12-sided polyhedron where each face is a pentagon twelve edge 512 (See details in Section 2.1.1). The hexsakaidecahedron is a 16-sided polyhedron with twelve pentagonal side surfaces and four hexagonal side faces, 512 64. The larges cavities of the SII are bigger than the large cavity of sI, and can accommodate larger guest molecules (Sloan and Koh, 2008). The smaller cavity of sII has cavity radius slightly less than that of sI (3.91 Å versus 3.95 Å respectively). This is probably the reason why pure nitrogen form sII instead of sI. The ratio between the molecular diameter of nitrogen and the sII small cavity diameter is probably closer to an ideal fit (cf. Davidson, 1971).

In contrast to the 46 water molecules in the sI unit cell, the unit cell of sII has 136 water molecules, arranged in lattice of 24 cavities, 16 small and 8 large.

The most common sII hydrate formers are is, propane and iso-butane which only can occupy the large cavity. In oil and the gas industry sII is the most common structure formed (Svartaas, 1994). This is also the most stable structure.

2.1.3 Structure H, sH

The third and last identified structure is structure H. H stands for hexagonal, which is the shape of the structure. SH consists of small, medium and large cavities. It occurs much less frequently than the other two, and in terms of stability it lies between sI and sII.

Until 1987, it was assumed that molecules larger than n-butane were not suitable to act as guest molecules for hydrate formation. Then J. Ripmeester and his group identified the new structure, SH (Ripmeester et al. 1987). SH requires two types of guest molecules to stabilize the hydrate structure; one help gas that fits into the small and medium cavities, and the structure H former that fits in the large cavities. The small cavity is still the dodecahedron, while the medium sized cavity is an irregular dodecahedron consisting of four square sides, six pentagonal lateral surfaces and three hexagonal sides, $4^3 5^6 6^3$, and has a radius of 4.06 Å. The large cavity is an irregular isocahedron - a 20 - sided polyhedron with 12 pentagonal and 8 hexagonal side faces, 512 68, with a radius of 5.71 Å (Sloan and Koh, 2008).

The unit cell of sH consists of 34 water molecules, arranged in 3 small, 2 medium and 1 large cavities.

The sI and sII may be formed in the presence of only one hydrate forming gas only, while structure of H forming component requires a help gas, e.g. methane, for the structure to form. SH-forming molecule are e.g. 2-methylbutane, 2,2-dimethylbutane, 2,3-dimethylbutane, 2,2,3-trimtylbutan, 2,2 - dimethyl pentane, 3, 3 dimethyl pentane, methyl cyclopentane, ethyl cyclopentan, methyl cyclohexan, cycloheptane and cyclooktane. These sH-forming molecules rarely occur in natural gas, and this could be the reason why sH occurs less frequently than sI and sII (Carroll, 2003).

2.2 Kinetics hydrate nucleation

Nucleation is perhaps the most challenging step in the understanding of the process of gas hydrate formation. Hydrate nucleation is a process where small, sub-critical embryonic clusters of water and gas continuously form and dissociates in an attempt to achieve a critical size for sustainable growth. The region where the formation and dissolution of such embryonic pre-hydrate structures occurs, with equal probability, is called a metastable region. On a micro scale this process involves between ten and a thousand molecules, and it is thus very difficult to observe experimentally. Current hypotheses for hydrate nucleation are based on known phenomena such as freezing water, gas dissolution in water and simulated data of both phenomena (Sloan and Koh, 2008).
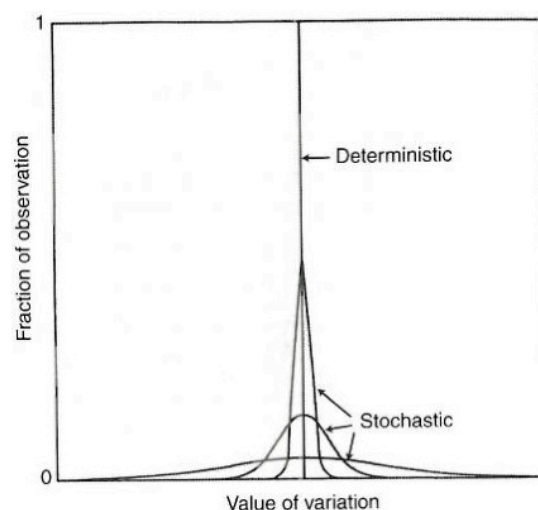
Figure 2.2: Comparison of stochastic and deterministic properties (Rowley, 1994)

Nucleation processes are in general stochastic. The difference between stochastic and deterministic features is illustrated in Figure 2.2. For a specific equilibrium state, the probability of observing a particular condition at given temperature is 1. The deterministic equilibrium condition involves negligible variation in the measured temperature. Stochastic behaviour is evident in the three lower curves in Figure 2.2. (Sloan and Koh, 2008)

If we look at the results from hydrate nucleation experiments in the laboratory the stochastic behaviour or the width of the variation as illustrated in Figure 2.2 is function of the experimental temperature. At temperatures close to equilibrium the distribution width of measured nucleation times may be very broad and appear as very stochastic, while at lower temperatures nucleation occurs more frequently and the process occurs as apparently less stochastic on the time scale.
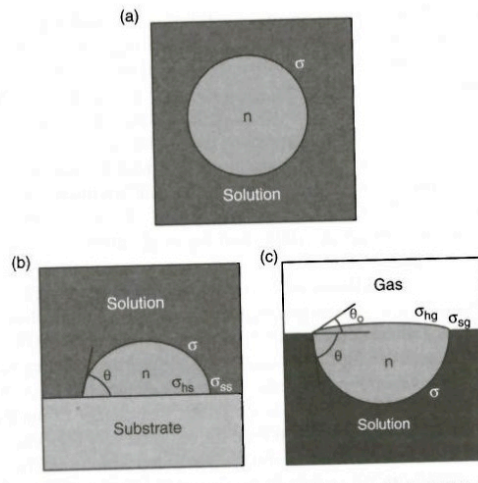
Figure 2.3: Schematic of (a) spherical cluster of n building devices is the HON, (b) hat-shaped cluster of n building units in 3D in HEN on a substrate, (c) Lens-shaped cluster of n building units in 3D in HEN the solution gas interface (ref. Kaschiev and Firoozabadi, *J.Cryst.Growth*, 243, p476)

Primary nucleation can be of a homogenous or heterogeneous type. Homogeneous nucleation occurs spontaneously in a solution and involves two phases only – the solution and the new phase being formed in the solution. This is illustrated in Figure 2.3 a. Heterogeneous nucleation involves three or more phases and occurs e.g. at the interface between gas, water and the forming hydrate (the new phase) as illustrated in Figure 2.3 c. Heterogeneous nucleation may also occur on the surface of a foreign particle added to the solution, at a metal surface or on the surface of a substrate as illustrated in Figure 2.3 b. The substrate will act as the third phase involved in the nucleation process.

2.2.1 Homogeneous nucleation (HON)

Homogeneous nucleation is rarely observed during hydrate formation. Nucleation commonly takes place at the hydrocarbon – water interface and not in the bulk of water. However, classical nucleation theory is based on the homogeneous case and homogeneous nucleation should be discussed to obtain a clear picture of the nucleation process. During nucleation in absence of impurities and the third phase there is a consolidation process occurring in solution. This means that there is a sequential formation of clusters of molecules that increase in size until it has reached a critical mass. This is illustrated in Figure 2.4 where embryonic clusters below critical size (left part of figure) are in a continuous growing / dispersing process (middle section of figure) until the first cluster reaches the critical size (right section of figure) and sustainable growth can commence. The critical size is the size of the cluster must be reached before the core / cluster can grow spontaneously. Before this critical size is reached clusters can either grow or shrink. This is a result of density or composition fluctuations. (Sloan and Koh, 2008)
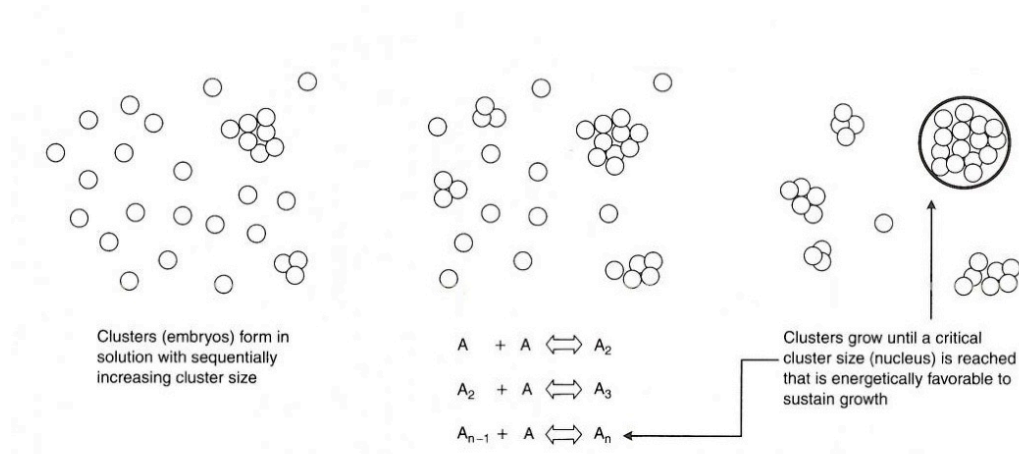
Figure 2.4: Schematic of the formation of a critical nucleus according to Classical Nucleation Theory (Sloan and Koh, 2008)

Once the cluster has reached critical mass, and it begins to grow spontaneously, we describe the process through the Gibbs free energy (Δ G) between a small particle of solute and solute in the solution. Δ G is equal to the sum of the surface excess free energy, Δ G$_s$ (the energy required to create additional surface and arrange the solute to be a part of the additional surface area) and the volume excess free energy, Δ G$_v$ (the energy released forming the new mass / additional volume created).

$$\Delta G = \Delta G_s + \Delta G_v = 4\pi r^2 \sigma + \frac{4}{3}\pi r^3 \Delta g_v \qquad (2.1)$$

Here is Δg_v the free energy change per unit volume and σ is the surface tension (of crystal-liquid interface). (Sloan and Koh, 2008)

Gribbs free energy for constant temperature can be expressed as: (Smith et al., 2005)

$$\Delta G = \Delta H - T\ \Delta S \tag{2.2}$$

At the beginning of the process, when the clusters start to grow, the entropy decreases and ΔS (the entropy) becomes negative. This is because it takes energy to structure and organize the water molecules in the right patterns, or so called lattice structures on the surfaces of the clusters. This indicates that there is disarray in the system at the beginning. To enable the clusters to continue growth, there must be sufficient excess energy released (feedback energy) to arrange new water molecules in lattice structures and maintain growth. The contribution of entropy is the structuring of the surface of the clusters and defined by ΔG_s, is a function of the cluster radius and surface tension in the area of contact / interface between the clusters and liquid. ΔG_s is given by:

$$\Delta G_s = 4\pi r^2 \sigma \tag{2.3}$$

where r is the cluster radius, and σ is the surface tension at the hydrate – water interface. ΔG_s is corresponding with $T\Delta S$ in equation (2.2).

Enthalpy (see section 2.3), ΔH, is the energy released through the exothermic process and corresponds to ΔG_v, which in turn is related to the volume of the clusters or the new crystal mass formed, and is given by:

$$\Delta G_v = \frac{4}{3}\pi\ r^3 \Delta g_v \tag{2.4}$$

Here is Δg_v the change in the free energy per unit volume of hydrate formed, and r is the cluster radius. In order to use this equation it must be assumed that the cluster is spherical and the volume can then be calculated as the volume of a normal sphere, $V = \frac{4}{3}\pi r^3$.
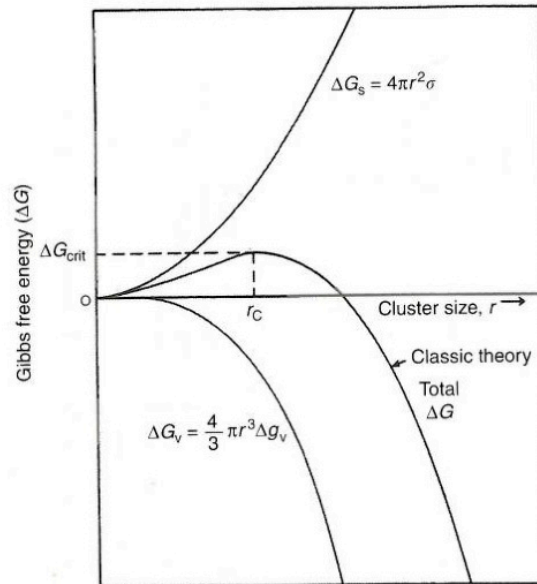
Figure 2.5: Comparison of surface excess free energy and volume excess free energy as functions of cluster size (Larson, 1989)

Figure 2.5 illustrates the relationship between the surface excess free energy, ΔG_s and the volume excess free energy, ΔG_v, as a function of cluster size, r. ΔG_s and ΔG_v are of opposite sign, and for very small particles / clusters the surface area is relatively large as compared to the volume and ΔG_s dominates and ΔG obtain a positive value indicating a process that cannot proceed self-sustained. The total ΔG, is the sum of ΔG_s and ΔG_v, has an apex called ΔG_{crit}. At this point ΔG_s and ΔG_v balances the spontaneous growth may commence. The radius of the cluster at the critical point is denoted r_c. At ΔG_{crit}, $\delta \Delta G/\delta r = 0$ and r_c can be found by differentiating equation (2.1): (Sloan and Koh, 2008)

$$\delta \Delta G/\delta r = 8\pi r\sigma + 4r^2\Delta g_v = 0 = 2\pi r_c\sigma + r_c^2\Delta g_v \qquad (2.5a)$$

which solved w.r.t. r_c gives:

$$r_c = -2\sigma/\Delta g_v \qquad (2.5b)$$

Rearranging equation (2.5b) to $\Delta g_v = -2\sigma/r_c$ and input equation 2.1 we obtain:

11

$$\Delta G_{crit} = \frac{4}{3}\pi \, \sigma r_c^2 \tag{2.6}$$

If ΔG_{crit} can be determined the critical radius can be expressed as:

$$r_c = \sqrt{\frac{3\Delta G_{crit}}{4\pi\sigma}} \tag{2.7}$$

2.2.2 Heterogeneous nucleation (HEN)

Mullin (1993) claimed that homogeneous nucleation was not a common occurrence, and that it was almost impossible to get to a solution completely free from foreign particles. Wyslouzil (1997) came to the same conclusion and supported Mullin's statement.

From all investigations done on the subject, it is concluded that in almost all cases of nucleation, the nucleation is heterogeneous. From the free energy point of view, the nucleation process is most likely to happen on a two-dimensional surface. That is, on a pipe wall or on a particle, and not on a three-dimensional surface (free volume of water). The angle of contact (θ) between hydrate crystal and a surface is related to ϕ. This is a fraction which is multiplied by the value of ΔG_{crit} for HON to giva a smaller $\Delta G'_{crit}$ for HEN: (Sloan and Koh, 2008)

$$\Delta G'_{crit} = \phi \, \Delta G_{crit} \tag{2.8}$$

$$\phi = [(2 + \cos\theta)(1 - \cos\theta)^2] / 4 \tag{2.9}$$

When the contact angle is $\theta = 180°$ (complete not damp from the substrate) is $\Delta G'_{crit} = \Delta G_{crit}$. If $\theta = 0°$ (complete damp) is $\Delta G'_{crit} = 0$

We also notice that foreign surfaces effectively lower the $\Delta G'_{crit}$ and the critical radius (r_c) that is required for spontaneous growth. This can be seen in the equations (2.8) and (2.9). HON of hydrates is a departure from this. Therefore HEN occurs much more frequently. (Sloan and Koh, 2008)

Kashchiev and Firoozabadi (2002) have analyzed the kinetics of nucleation of one-component gas hydrates in aqueous solutions. The expression was derived for the stationary frequency of hydrate nucleation; J, for HEN on the solution gas interface or on a solid surface, and also the

special case of homogeneous nucleation. Their work on the kinetics of hydrate nucleation provides a detailed examination of the mechanisms and kinetics expression of hydrate nucleation, based on the classical nucleation theory. The work W (J) required to forms a hydrate cluster of n building units, which may be subsequently determined by the classical theory of nucleation: (Sloan and Koh, 2008)

$$W(n) = -\ n\ \Delta\mu + C\nu_h^{2/3}\ \sigma_{ef}\ n^{2/3} \qquad\qquad (2.10)$$

Here $\Delta\mu$ is the supersaturation. Physically, this term represents the work obtained through the mounting of n hydrate building unit into an n-size hydrate cluster (nucleation can only occur when $\Delta\mu > 0$). C is the form factor. A spherical cluster is formed in HON (C = $(36\pi)^{1/3}$ / 3 ; See Figure 2.3). In HEN is a hat-shaped cluster formed on a substrate surface, while a lenticular grid formed at the interface between the solution and the gas phase (figure 2.3 b and c). The volume of the hydrate building unit, ν_h (m^3), consists of one molecule of gas and n_w (hydration number) water molecules. The effective specific surface energy, σ_{ef} (J/m^2), is the work done to produce the interface between the cluster and the solution (in HON), or the solution and the substrate (HEN), or the solution and gas (HEN). (Sloan and Koh, 2008)

2.3 Enthalpy

Enthalpy gives an expression for of the amount of heat emitted or taken up by a process, and carries the symbol H. A system has a constant or given enthalpy, but when there is temperature change (internal energy) or a chemical reaction the system enthalpy will be changed either due to heat added, heat lost or heat produced. The enthalpy change, ΔH, of a reaction is expressed by:

$$\Delta H = H_{pro} - H_{reac} \qquad\qquad (2.11)$$

H_{pro} = formation enthalpy of products
H_{reac} = formation enthalpy of reactants

By definition the formation enthalpy of elements in their natural state is set to zero.

Heat capacity at constant pressure, c_p, is defined by:

$$c_p \equiv \left(\frac{\partial H}{\partial T}\right)_p \qquad (2.12)$$

If heat is released, the process is called an exothermic reaction, and by definition $\Delta H < 0$ for exothermic processes. Displaying an opposite reaction, namely that the process requires energy input (heat), the process is known as an endothermic reaction, and for endothermic processes $\Delta H > 0$.

For adiabatic processes without heat loss to the surroundings all energy release will be stored in the volume and the enthalpy change can be determined from the temperature change in the product and its heat capacity. For process with heat loss, formation enthalpy can be estimated if the heat loss rate is known.

There have been conducted several studies on the formation enthalpy of different gas hydrate systems at different temperatures and for different gas compositions. Lievois (1987, PhD Thesis) gave some results from his experiments on formation enthalpy with pure methane. These results are shown in Table 2.1 below:

Table 2.1: Enthalpy with constant pressure and methane (Lievois, 1987).

T [K]	ΔH [J/gmol] (CH_4)
278.2	57.739
278.2	57.358
278.2	57.697
283.2	52.798
283.2	53.610

Based on his experiments, we can see that at 5 ° C the enthalpy is estimated in an excess of 57.5 J / g mol, and when the temperature rises to 10 ° C the enthalpy decreases to about 53 J / g mol. So according to Loevois (1987, Lievois) the formation enthalpy decreases as function of increasing temperature.

Graydon K. Anderson (2004, Anderson) tried to gain a better understanding of the enthalpy of formation (= melting enthalpy). He did this by measuring the formation enthalpy of methane hydrate over a wide range of temperatures from 274 to 318 K (see Table 2.2). From his results it appears that the enthalpy is relatively constant around 53-55 kJ/mole over the entire temperature range.

Table 2.2: Enthalpy change of reaction (1) and hydration number from 274 K to 318 K (Anderson, 2004)

T/K	p/MPa	dp/dT $(MPa \cdot K^{-1})$	x_{CH_4}	ΔV $(m^3 \cdot mol^{-1})$	$\Delta H_{1a}(T,p)$ $kJ \cdot mol^{-1}$	$\Delta H_{1b}(T,p)$ $kJ \cdot mol^{-1}$	$\Delta H_1(T,p)$ $kJ \cdot mol^{-1}$	ΔH_1^* $kJ \cdot mol^{-1}$	n
274	2.85	0.270 ± 0.007	0.00115	$7.16E-04$	52.9 ± 1.3	0.132	53.0 ± 1.3	52.9 ± 1.3	5.89 ± 0.22
278	4.28	0.414 ± 0.011	0.00146	$4.60E-04$	52.9 ± 1.4	0.158	53.1 ± 1.4	52.3 ± 1.4	5.79 ± 0.23
282	6.36	0.660 ± 0.0020	0.00181	$2.91E-04$	54.2 ± 1.5	0.185	54.4 ± 1.5	53.1 ± 1.5	5.93 ± 0.26
286	9.88	1.150 ± 0.037	0.00229	$1.69E-04$	55.5 ± 1.7	0.217	55.7 ± 1.7	54.3 ± 1.7	6.12 ± 0.28
290	16.06	2.016 ± 0.069	0.00286	$9.15E-05$	53.5 ± 1.7	0.259	53.7 ± 1.7	52.5 ± 1.7	5.83 ± 0.29
294	26.69	3.39 ± 0.12	0.00349	$5.27E-05$	52.5 ± 1.8	0.287	52.8 ± 1.8	51.8 ± 1.8	5.71 ± 0.30
298	43.92	5.31 ± 0.21	0.00419	$3.39E-05$	53.7 ± 1.9	0.294	54.0 ± 1.9	52.9 ± 1.9	5.90 ± 0.32
302	69.68	7.62 ± 0.31	0.00499	$2.36E-05$	54.2 ± 2.0	0.294	54.5 ± 2.0	53.7 ± 2.0	6.02 ± 0.34
306	105.18	10.17 ± 0.44	0.00583	$1.75E-05$	54.5 ± 2.2	0.266	54.8 ± 2.2	53.2 ± 2.2	5.94 ± 0.36
310	151.70	13.28 ± 0.60	0.00661	$1.32E-05$	54.4 ± 2.3	0.200	54.6 ± 2.3	52.6 ± 2.3	5.85 ± 0.38
314	214.40	18.74 ± 0.89	0.00723	$9.29E-06$	54.7 ± 2.4	0.081	54.7 ± 2.4	52.5 ± 2.4	5.83 ± 0.40
318	311.12	31.6 ± 1.6	0.00744	$5.45E-06$	54.7 ± 2.6	-0.114	54.6 ± 2.6	52.5 ± 2.6	5.82 ± 0.44

Comparing the two different researches, we see that the results are fairly similar, only that Loevois (1987, Lievois) is slightly higher and has a decreasing trend as function of increasing temperature in his results, while Andersons results remain constant over an even wider temperature range.

2.4 Hydrate Crystal Growth Processes

There are different types of hydrate crystal growth processes. They can be divided into four main types (Sloan and Koh, 2008):

(1) Single crystal growth
(2) Hydrate film/shell growth at the water-hydrocarbon interface
(3) Multiple crystal growth in an agitated system
(4) Growth of metastable phases

Type (1) and type (2) processes are most relevant for the present MSc work. That means; in the next two sections single crystal growth and hydrate film/shell growth at the water-hydrocarbon interface will be reviewed. (For the other two processes, it is referred to the book

"Clathrate Hydrates of Natural Gases" by E. Dendy Sloan and Carolyn A. Koh, 2008, chapter 3.2.2.)

2.4.1 Single crystal growth

Hydrates can grow in different ways, and singles crystals in water-hydrocarbon solution is one. This type of growth occurs most often in states with low driving force conditions. For example, to investigate the effect of additives on hydrate crystal growth and morphology, this is the most frequently experimental process used.

Single hydrate crystals of tetrahydrofuran (THF, sII hydrate) and ethylene oxide (sI hydrate), can be easily made in the laboratory and isolated for structural analysis. Both chemicals are completely soluble in water and hydrates can be formed at atmospheric pressure at temperatures above the freezing point of water. In contrast; single crystals of gas hydrates are much more difficult to produce and isolate, and only a few studies have been able to obtain single crystals of gas hydrates for structural analysis.
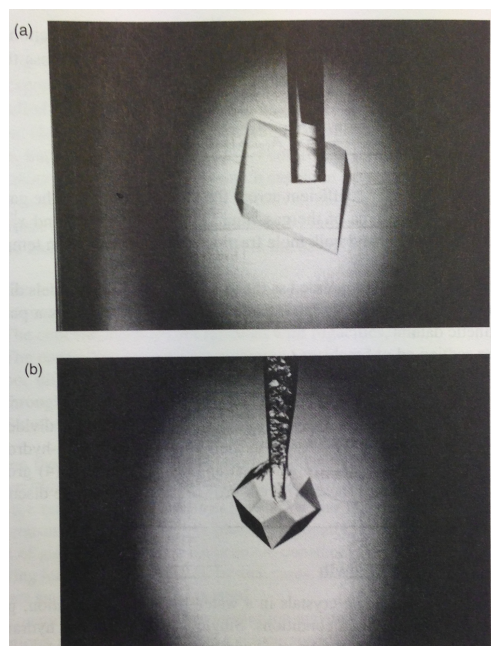
Figur 2.6: Photograph of single hydrate crystals of (a) tetrahydrofuran (sII), (b) ethylene oxide (sI) (Sloan and Koh, 2008)

If we take a look at figure 2.6 a and b, we can see single hydrate crystals of structures I and II. On picture (a) we see a structure II hydrate grown from stoichiometric solution of THF. Picture (b) shows a structure I hydrate that is grown from a stoichiometric solution of ethylene oxide, respectively, in resting conditions. These single crystals show exhibits (110)

and (111) crystal planes of structure I and II respectively. It is very important to know that in single crystal growth it is the slowest growing planes that are observable, while the fast growing planes are rapidly disappearing. Smelik and King (1997) arrived at similar figures in terms of single crystal growth through their high-pressure single crystal system.

From all the studies on this subject Smelik and King comes up with a hypothesis that the (111) planes in SII are the slowest growing. This comes from the fact that it consists of the predominance of hexagonal face compared to the other crystal planes in SII. The reason that these crystal planes containing the predominance of hexagonal face grows slower than the others is because they is considerably more strained (120 ° between O-O-O angles) than those pentagonal faces (108 °), with respect to either tetrahedral O-O-O angle (109 °) or water angle (H-O-H of 104, 5 °). Also the (110) plane of the SI crystal has a similar argument. (Sloan and Koh, 2008)

2.4.2 Hydrate film/shell growth at the water-hydrocarbon interface

Hydrate nucleation and growth is usually initiated at the water-hydrocarbon interface. Measurements of the growth of a hydrate film (or shell) at of the water-hydrocarbon interface provides insight into the growth mechanism(s) which may be incorporated in realistic hydrate growth models. Table 2.3 summarizes the various studies which have been conducted on the growth and morphology of a hydrate film / shell at the water-hydrocarbon interface (where the hydrocarbon may be gaseous or liquid). (Sloan and Koh, 2008)

Table 2.3: Experimemtal Studies of Film/Shell Growth at the Water-Hydrocarbon (Sloan and Koh, 2008)

Hydrate film/shell measurement	Water-hydrocarbon interfacial system	Research group(s)
Film growth at liquid water-hydrate former interface	Water-methane	(Smelik and King, 1997) (Makogon et al., 1998) (Freer et al., 2001) (Taylor, 2006)
Film growth at liquid water-hydrate former interface	Water-fluorocarbon	(Sugaya and Mori, 1996) (Ohmura et al., 2000) (Ito et al., 2003)
Film growth at liquid	Water-carbon dioxide	(Uchida et al., 1999b)

water-hydrate former interface		(Hirai et al., 2000) (Mori, 2001) (Uchida et al., 2002) (Hirai and Sanda, 2004)
Shell growth on gas (hydrate former) bubble surface	Natural gas bubble in salt water	(Maini and Bishnoi, 1981) (Topham, 1984)
Shell growth on gas (hydrate former) bubble surface	Air bubble-ice interface	(Salamatin et al., 1998)
Shell growth on gas (hydrate former) bubble surface	Hydrofluorocarbon gas bubble in water	(Nojima and Mori, 1994)
Shell growth on liquid hydrate former droplet surface	Hydrofluorocarbon droplet in water	(Kato et al., 2000) (Ohmura et al., 1999, 2003)
Shell growth on liquid hydrate former droplet surface	Cyclopentane droplet in water	(Taylor, 2006)
Shell growth on liquid hydrate former droplet surface	Liquid carbon dioxide droplet in water	(Shindo et al., 1993)
Shell growth on droplet surface of aqueous solution of hydrate former	Aqueous THF solution droplet in n-decane	(Taylor, 2006)
Shell growth on water droplet surface	Water droplet in methane or carbon dioxide gas	(Servio and Englezos, 2003a) (Moudrakovski et al., 2004)
Shell growth on water droplet surface	Water droplet in fluorocarbon gas	(Fukumoto et al., 2001)

Several of these studies show similarities and one of the conclusions are that morphological changes are generally the same regardless of the hydrate former. That is, saturation (or the driving force) has an effect on morphology, and there are similarities between growth behaviour at a water-hydrate former planar interface and at the surface of a liquid droplet.

Servio and Englezos (2003) studied the effect of the pressure force on the morphology of methane and carbon dioxide hydrates grown from droplets of water at 5 and 2.5 mm in diameter immersed in a hydrate-forming gas atmosphere. To prevent the water droplets wetting the surfaces, they were laid on a Teflon coated surface of stainless steel. In every experiment two or three droplets of water were used in the crystallizer tank. As early as during the first five seconds after core formation at high driving force, the result could be seen. The surface of the droplet appeared roughened and dull with many fine needle-like crystals extruding away from the gas hydrate-water interface, see figure 2.7. This morphological discovery that Servio and Englezos did was also the same for methane and kabon dioxide hydrate former gases.
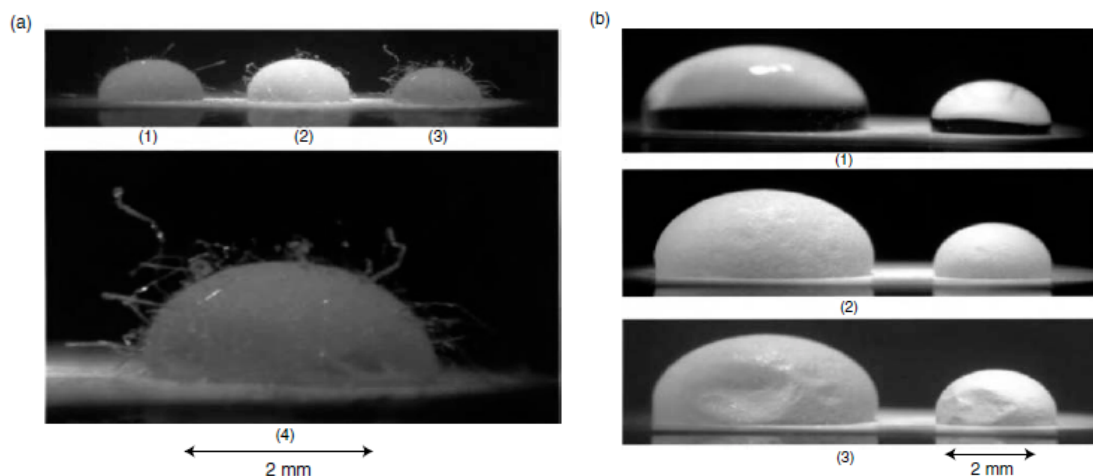
Figure 2.7 (a) Methane hydrate covering the surface of water droplets (1, 2, 3) under high driving force, 10 min after nucleation. Image (4) is a magnified view of droplet (3), and (b) methane hydrate covering two water droplets under low driving force at three different times: (1) at *t* = 0, (2) at *t* = 10 h where the water droplet is covered by hydrate, (3) at *t* = 25 h where the water droplet is covered by hydrate and depressions in the hydrate layer appear. (Servio and Englezos, 2003).

Based on their experiments Sevio and Englezos (2003) suggested that with high driving force applied on the system the hydrate consists of three growth phases:

1. The appearance of a hydrate layer (shell) around the water droplet with needle-like crystals, and up to 10 h after nucleation the needle-like crystals grow in size and thickness
2. The crystal needles collapse onto the hydrate layer covering the droplet
3. Appearance of depressions in the hydrate layer surrounding the water droplet, which occurred within 10-15 h to a couple of days in some experiments.

At high driving force it is hard to control where the hydrate will grow, because it can grow and multiply in so many different places. However, at low driving force the growth behaviour was totally different; the hydrate is more predictable, in both grow and location.

The difference between high and low driving power can be seen in figure 2.7 a and b. A is the picture of a droplet at high driving power and b of a droplet at low driving power. At the droplet on picture b there are no signs of crystals on the surface, just a smooth and shiny texture. The reason for this is difficult to say, however, it has been suggested that it is because when high force is produced a greater number of core element areas are produced compared with low force. This fits well with the proposal that came with Mullin in 2001 that the rate of nucleation, or easily explained, that the number of nuclei formed per time per unit volume increases with the degree of supersaturating. Supersaturating turn is proportional to the driving force. This means that where there is a high driving force is where the core of many sites are present with core items faster kinetics and therefore may result in more random crystal growth and thus a rougher surface.

2.4.3 Correlations of the Growth Process
In table 2.4 it is summarized the different hydrate growth models that is most commonly used and referred to in the literature. Various research groups have studied the different models in their laboratories and three main correlations for hydrate growth can be extracted: (Sloan and Koh, 2008)
1. Intrinsic growth kinetics
2. Mass transfer limited
3. Heat transfer limited

Later in this chapter, various models from each correlation mentioned above are presented, with a brief critique. It is important to use the kinetic models with great care for the following three reasons: (Sloan and Koh, 2008)

1. Hydrate nucleation is a stochastic process (as mentioned in previous chapters means that there is great variation in the data at low driving force in isothermal conditions).

2. Each model is made artificially formed hydrates, and relies on some power juicer. And it is not always certain that what's happening in the labs can be compared with what happens in the real nature.

3. In the literature are most of the data determined for sI hydrates, even if we know that natural gas typically forms sII hydrates.

Table 2.4: A summary of the Different Hydrate Growth Models (Sloan and Koh, 2008)

Growth model	Driving force/model features	Researchers
Growth kinetics	$(f-f_{eq})$	(Englezos et al., 1987 a,b)
Growth kinetics	$(f-f_{eq})$ Minor modification to Englezos' model	(Malegaonkar et al., 1997
Mass transfer	$(x^i_{int} - x^i_b)$ Simplification/modification to Englezos' model	(Skogborg and Rasmussen, 1994)
Mass transfer	Based on phase field theory	(Svandal et al., 2005)
Mass transfer	Based on Monte Carlo cellular automata	(Buanes et al., 2006)
Heat transfer	Curved film front growth on water-hydrate former interface	(Uchida et al., 1999a)
Heat transfer	Curved film front growth on water-hydrate former fluid interface	(Mori, 2001)
Heat transfer	Straight film front growth on water side of water-hydrate former interface	(Freer et al., 2001) (Mochizuki and Mori, 2006)

2.4.3.1 The Englezos-Bishnoi model

Englezos conducted several hydrate growth kinetic experiments on methane and ethane and also a mixture thereof. He suggested a kinetic model in (1987) based on the assumption that hydrate formation is composed of three steps: (Sloan and Koh, 2008)

1. Transport of gas from the vapor phase to the liquid bulk phase
2. Dispersion of gas from liquid bulk phase through the boundary layer around hydrate particles
3. A reaction involving the adsorption gas molecules to be incorporated in the structured water framework atthe hydrate interface

Over the years old technology has been tested and methods and models have been improved by tuning the model to the growth rate per particle taking the high solubility of carbon dioxide in water into account, Englezos' kinetics model was described as follows:

$$(dn_i/dt)_p = K \cdot A_p \ (f_i^b - f_i^{eq}) \tag{2.13}$$

with

$$1/K^* = 1/k_r + 1/k_d \tag{2.14}$$

where

$(dn_i/dt)_p =$ number of gas moles consumed per section by the hydrate

$A_p =$ the surface area of each particle

$f_i^b =$ fugacity of component i in the bulk liquid

$f_i^{eq} =$ equilibrium fugacity of component i in the liquid at the hydrate interface

$K^* =$ hydrate formation growth rate constant, representing a combined rate constant for diffusion (mass transfer) and adsorption (reaction) processes

$k_r =$ reaction rate constant

$k_d =$ mass transfer cowfficient through the film around the particle

$(f_i^b - f_i^{eq})$ defines the overall driving force in Englezos work.

It is well realized that, as with any model, that there are limitations and restriction connected to general use. According to Sloan and Koh (2008) it is assumed that intrinsic kinetics typically is less important in hydrate formation in real systems involving turbulent mixing (e.g. pipelines) and mass and heat transfer may be more important in "real life" situations. Thus for the present MSc thesis we have been more focused on models based on heat and mass transfer.

2.4.3.2 The Skovborg-Rasmussen model

After analysing the Englezos – Bishnoi model, Skovborg and Rasmussen's attempt rediscovered changes that could simplify a kinetic model and noted two restrictions for the Englezos – Bishnoi model:

1. The secondary nucleation constant was very low, 10^{-3}. This means that there is no secondary nucleation, and that the Englezos – Bishnoi model assumes that all the particles are of the same size and grows with the same rapidity. This resulted in Skovborg and Rasmussen choosing to remove crystallization population balance from the model.

2. K * value seems to be too high. If this is correct, it will give error in the mass transfer factor through the liquid film k_L. K_L values obtained solubility without forming hydrate, which can lead to errors. If it is found that certain k_L values are wrong, it will have a major impact on K *. 50% error on k_L leads to the two orders of magnitude errors in K *.

Skovborg and Rasmussen proposed the following model to describe hydrate growth rate:

$$dn/dt = k_L A_{(g-1)} c_{wo} (x_{int} - x_b) \qquad (2.15)$$

where

$A_{(g-1)}$ = Gas-liquid interface area

c_{wo} = initial concentration of water

x_{int} = bulk liquid mole fraction of the component

2.4.3.3 Heat transfer models

There are several, different models based on heat transfer to describe hydrate growth. In figure 2.8 a) to d shows various models for the lateral growth of hydrate film on the water-gas interface. The first one is Uchida's model from 1999 (Figure 2.8 a). He performed experiments on the surface of water droplets submerged in liquid carbon dioxide. The experiments showed that the hydrate crystal only was formed at the front of the hydrate film. A three-phase equilibrium temperature maintains this front. These three phases are water, guest liquid and hydrate. It was further assumed that the heat transfer from the front to the water and guest solvent was continuous batch, and that there is an exothermic process in which it is envisaged that the heat that is removed from the front is balanced with the heat generated by hydrate. Out of all this, Uchida found that the linear growth rate of hydrate film along the interface, ν_f, the hydrate film thickness, δ, and the degree of subcooling, ΔT. δ is determined by plotting the calculated ν_f - ΔT against the experimental data.

During the 2000's several researchers were sceptical about how realistic and accurate the model of Uchida really was. Could the relatively simple reports explain reality, explain how the hydrate actually behaved? Mochizuki and Mori voiced their scepticism in 2005-2006. They believed that the major problem was the design that Uchida gave the conductive heat transfer from the film front. This had little physical reasoning. Mochizuki and Mori meant that the direct measurements of the hydrate film thickness under pressure are much harder than the lateral film growth measurements Uchida conducted. This led to Uchida model went from a model to be a method for determining hydraulic minority film thickness.

Prior to improvements on the Uchida model as suggested by Mori and Mochizuki in 2005 and 2006 Mori had already published a model based on heat transfer in 2001. Mori's model from 2001 is illustrated in Figure 2.8 b). This model is based on lateral growth of hydrate film on the interface between the water that is stationary and a guest solvent. As in Uchida model the heat of hydrate is also released in the moving front, whereas in Mori's model the heat is assumed removed away from the front to the liquid phase of a steady convective heat transfer. But in opposition to Uchida; Mori suggested a countercurrent flow, which occurs at a velocity of opposite sign but with the same speed as the film front. This means that this model could give better agreement with the experiments for ν_f - ΔT relationships than the model described in the first two paragraphs.

Figure 2.8 c shows Freer's model from 2001. This is a model that is based on data obtained from experiments on methane hydrate film growth rate at methane-water interface. It has been predicted that there is a one-dimensional conductive heat transfer from the front of the film to the water phase that extends beyond the front. This in turn provides data that can model the v_f values. However, the calculations that were done gave Freer much lower v_f values than he got from the experiments. Based on this conclusion; Freer claimed that the hydrate film growth can be controlled by kinetic hydrate formation. Mochizuki and Mori came with a suggestion that since hydrate films are basically very thin fronts are most likely convex contours with strong curvatures, rather than straight-edged.

Finally, it is the latest model to Mochizuki and Mori is from 2006 and is shown in Figure 2.8 d This model has many similarities with Freer's model, which both show that the hydrate film is believed to exist on the water side of the water-guest interface. Furthermore assumes that hydrate film has to be homogeneous from a macroscopic scale, and the water and guest phases extended infinitely. Mochizuki and Mori worked on to look at the speed of growth, and assumed that the lateral hydrate film growth was significantly faster than film thickening / thinning. Having made countless many attempts, they came to the conclusion that only hydrates forms at the front of hydrate film and that temperature the front maintained by three-phase equilibrium temperature. There are no guest or water movements and the speed of heat removal from the front is balanced by the rate of heat generation by hydrate formation.

The linear growth rate of the hydrate film along the water/hydrocarbon (hydrate former fluid) interface, v_f, is given in Equation (2.14). v_f is the same as $\frac{dx_h}{dt}$.

$$\rho_h \delta \Delta h_H v_f = \int_0^\delta (\lambda_h \frac{\partial t}{\partial x}\Big|_{X=x_h-} - \lambda_w \frac{\partial t}{\partial x}\Big|_{X=x_h+}) \, dy \qquad (2.16)$$

δ is the hydrate film thickness, $\frac{\partial t}{\partial x}\Big|_{X=x_h-}$ and $\frac{\partial t}{\partial x}\Big|_{X=x_h+}$ gives the hydrate-side and the water-side temperature gradients where x = x_h (the x position of the hydrate-film front), Δh_H gives the heat of hydrate formation per unit mass of hydrate and λ_h and λ_w are the thermal conductivity of hydrate and water, respectively (Sloan and Koh, 2008).

(a)

Conductive heat transfer

Hydrate film
(adiabatic film)

Hydrate film growth

r_h

Hydrate film model by Uchida et al. (1999)

(b)

Convective heat transfer

Flow

Water

Hydrate film
(adiabatic film)

Interface

Hydrate film growth

Flow

Hydrate-forming fluid

Hydrate film model by Mori (2001)

(c)

Hydrate film growth

Hydrate-forming fluid

Interface

Hydrate film
(adiabatic film)

One-dimensional
heat transfer

Water

Hydrate film model by Freer et al. (2001)

(d)

y

Water

Hydrate film growth

Conductive
heat transfer

δ

Hydrate film

Interface

0.

x

x_h

Hydrate-forming fluid

Adiabatic wall

Hydrate-forming site
Heat from hydrate formation is
generated here
Temperature is equal to T_{tri}

Figur 2.8: Hydrate film model by Mochizuki and Mori (Sloan and Koh, 2008)

2.5 Transient Heat transfer and heat transfer models

As part of an on-going hydrate project a simulation model has been developed by associate professor Runar Bøe (Dpt. of Petroleum, UiS) in an attempt to describe hydrate growth via heat transfer and energy balances. The principle for the model is as follows:

1. The temperature difference between the interior of the cell exposed to hydrate formation and energy production and the exterior of the cell exposed to the cooling water is utilized to estimate the energy flow across the cell wall. Input parameters are:
   a. Heat transfer coefficient between the water and cell wall at the interior surface (estimated using literature data and boundary layer theory, turbulent flow assumed).
   b. Heat conductivity through the titanium cell wall (described in literature).
   c. Heat transfer coefficient between the cooling water and cell wall at the outer surface (estimated using literature data and boundary layer theory and flow at the transition between laminar and turbulent).
2. The heat flow out of the cell must equal the sum of the enthalpy production by hydrate formation and enthalpy changes of the water, gas and the hydrate masses inside the cell due to temperature changes.
   a. The enthalpy content of the phases inside the cell can be calculated from the heat capacities of the various phases, their mass and the temperature.
   b. Adding the enthalpy change of the mass phases inside the cell to the heat flow out of the cell, the heat flow into the cell is determined. The heat flow into the cell must equal the released formation enthalpy by hydrate formation.
   c. The number of moles methane consumed during the same period can be found from the gas flow required to maintain constant pressure in cell during the hydrate formation process.
   d. Relating the number of moles methane consumed to the estimated energy produced in the cell, a formation enthalpy for methane can be determined.

Radial heat flow is assumed since both cells are cylindrical and cooled at the outer wall surface. For simplicity heat loss through the top lid section is neglected. The radial heat flow from the interior of the cell and to the cooling water through the wall is illustrated in Figure 2.9 a) while the figure in b) shows radial coordinates from above.
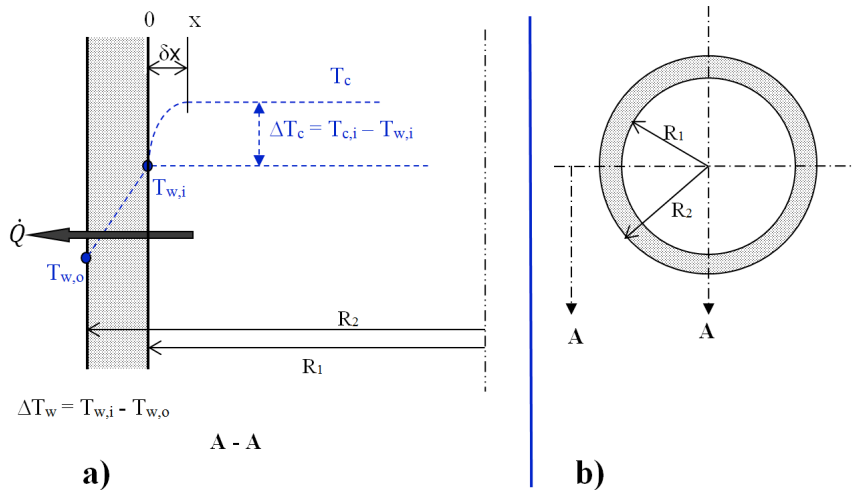
Figure 2.9: Figure showing heat flow out of the cell set up by temperature differences between the inside and outside.

The total heat transferred must be the same across all boundaries in radial direction, thus we can simplify the system by looking at the effect of the heat transfer coefficient at the inner boundary layer between the wall and the water bulk phase only and the temperature difference across the cell. In cell without hydrates formed the boundary layer at the inner surface will be function of the fluid flow along the surface, i.e. a function of the stirring rate. When hydrates form the inner boundary layer and the heat transfer properties through the liquid suspension of water and hydrates will be affected by the hydrates formed and how they behave in the cell (suspended as particles versus precipitated on the wall. Boundary layer on the inner wall affected by hydrates is illustrated in Figure 2.10.
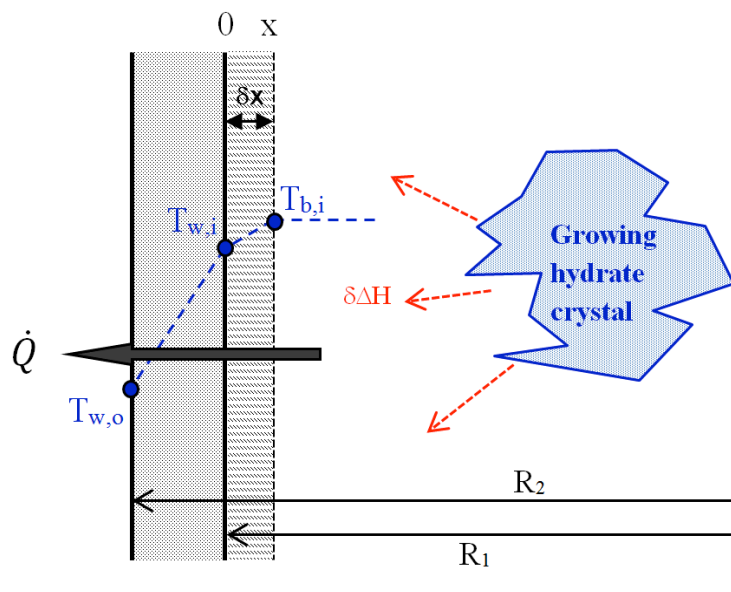
Figure 2.10: Figure showing illustrating the heat production (inflowing energy), the heat transport across the cell wall and a hydrate – water boundary layer at the inner cell wall.

The heat of reaction, $\dot{q}_R$ (dDH in Figure 2.10), can be expressed through a heat balance according to:

$$\dot{q}_R = \left(m_w \cdot c_w + N_g \cdot c_{p,g}\right)\frac{\partial T}{\partial t}\bigg|_I + h_I \cdot A_0 \cdot (T_I - T_0) \qquad (2.17)$$

where m_w is mass of water, c_w is heat capacity of water, N_g is mole of gas, $c_{p,g}$ is gas heat capacity, $\frac{\partial T}{\partial t}\big|_I$ is the inner temperature gradients, h_I is heat transfer coefficient across boundary layer at the inner cell wall, A_0 is the outer wall surface and $(T_I - T_0)$ is the temperature difference across the wall.

Balancing heat production by hydrate formation versus heat loss and amount of gas added to the cell during hydrate growth, the enthalpy of formation could be estimated. In the present work a model programmed in MatLab by associate professor Runar Bøe at the Department of Petroleum has been used for simulations. The use of this model simulator is described under method in Chapter 3 and the MatLab programme is added in Appendix E.

3 EQUIPMENT AND METHOD

In this present study, methane hydrate is produced in two different cylindrical cell reactors and gas consumption and heat release by hydrate formation measured. The methane hydrate was formed using pure water and scientific grade 5.5 methane. No other chemicals or fluids that could interfere with growth rates were present in cell during experiments. The only variables were the amount of water, the size of the cell, agitation speed and the experimental temperature. The pressure was maintained constant at 90 bara during all experiments.

The cell reactors were connected to a gas container via pressure control valve to maintain stable and constant pressure throughout the experiment, a flow meter was used to register the flow, a cooling bath was used to adjust conditions to the desired experimental temperature and Lab View® was used for data logging and data were stored on a computer. During experiments LabView could present the desired experimental data and progress on the computer screen. The experimental cell setup is presented in section 3.1.

Onset of hydrate formation during the experiment could be visualized on the screen through simultaneous changes in both the gas flow and the cell temperature.

In Subchapter 2.2 describes nucleation as a stochastic process; i.e. experiments run under the same conditions will not form hydrates at exactly the same induction time or start at the same spot in the cell during the experiments. Analysis of nucleation rates must thus be based on probabilities and probability distribution functions, but nucleation studies were not part of the present work and are not included herein. Growth kinetics is assumed less stochastic, but experimental measurements could be influenced by the stochastic nucleation process or the possibilities of keeping formed hydrate particles dispersed in a water suspension or being precipitated on equipment surfaces or agglomerated in larger lumps with total surface area differing from that of an ideal particle suspension. Agglomeration and precipitation would most probably affect heat transfer rates, total heat conductivities and affect the heat transfer from interior of the cell and to the cooling liquid. To establish the "optimal" experimental method for the study, the system with possible methods must be analysed to reveal undesired effects by method or other experimental parameters.

When hydrates start forming in the cell, we see that both the gas flow rate and the temperature rate (both in the water and gas) increases rapidly rises sharply and suddenly (see figure 3.1). The gas flow increases because the methane gas in the cell is used in the hydrate formation process and it must therefore be reloaded methane to keep the pressure constant. The hydrate formation is completed when the flow and temperature levels are down to the baseline levels again.
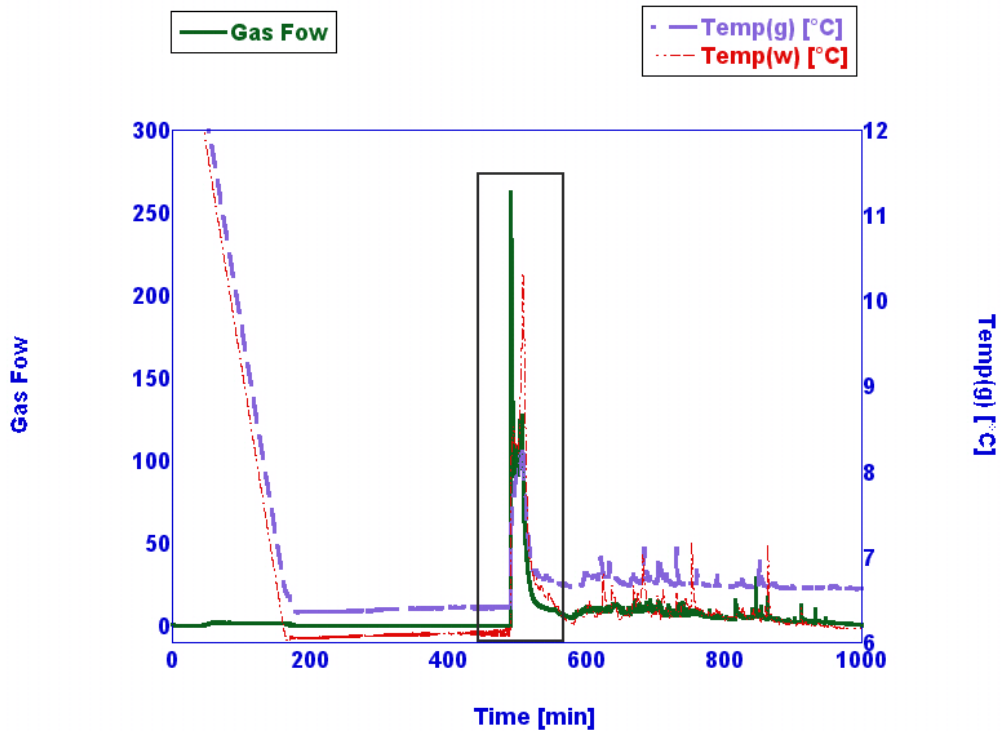
Figure 3.1: Typical graph of an experiment, gas flow and temperature (water and gas) vs. time. We can see where the hydrate is forming.

Each experiment at each set of experimental conditions (water volume, stirring rate) should have been reproduced 5 - 10 times or more to improve accuracy of analysis. But due to the limited time during the MSc thesis work; only 3 parallels at each experimental condition were normally conducted. If one of the three experiments within each experimental condition showed great deviations from the other two a fourth parallel was run to examine whether the observed deviation could be due to undefined problems during experiment. During some of the experiments there were larger discrepancies between recorded data and we have assumed deviations of 20 – 30 % as acceptable for this type of experiments.

3.1 The experimental setup
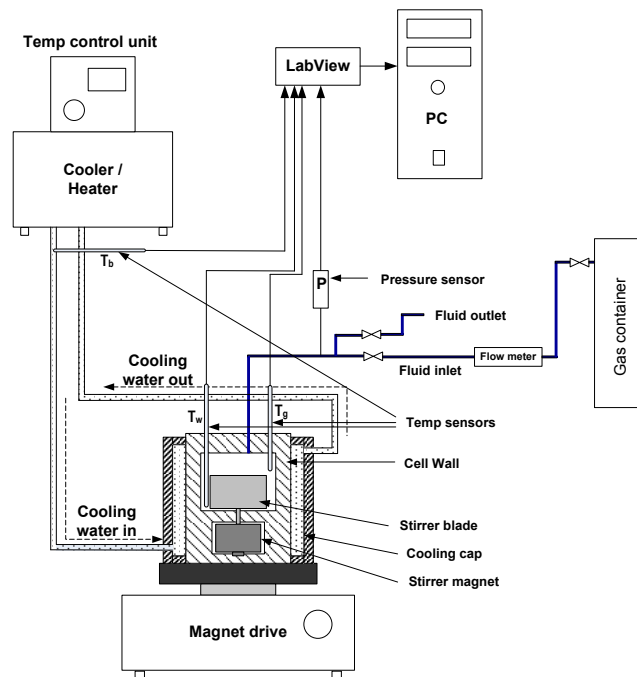
Figure 3.2: A sketch of the system used in the experiments. (Svartaas, 2013)

3.1.1 Test cell

The test cell that is used to perform experiments is a titanium cell developed at IRIS by Thor Martin Svartås (now UiS) and Einar Tostensen. As shown in Figure 3.3, the cell consists of a cell bottom lid, a magnet holder with mounted bearings, stirring blade, main cell, cooling jacket, circulation links, a cylinder head and a nylon ring. The whole cell is placed on a magnetic stirrer, allowing it to be stirred evenly throughout the experiment.

The stirring blade is screwed into the magnet holder, which consists of a powerful magnet. Under the magnet holder, between the magnet and the bottom lid, a nylon ring is inserted. This nylon ring is designed to prevent wearing on the tool. Around the cell is there a cooling jacket in hard plastic. Inside this there is a cavity in which the fluid regulates the temperature pumped through. Two 1/10 DIN Pt-100 temperature sensors with an accuracy of ± 0.03 °C, are mounted through Autoclave connections in the top lid. Both sensors are placed between the edge of the stirrer blade and the cell wall at approximate 2 mm distance from the wall. One of the sensors is placed in the upper section of the cell with the sensor tip approximately 20 mm below the top lid and records temperature in the gas phase. The tip of the second sensor is placed approximately 5 mm above the cell bottom and records the temperature of the

water and water – hydrate suspension during experiments. The accuracy of temperature readings are believed to lie within ± 0.1 °C. The top lid has a third Autoclave connection for gas supply via tubing from the container via the flow meter. A Rosemount 3500 TA absolute pressure transmitter is mounted in the gas supply line and pressure is read to an accuracy of 0.2 bara. It is important that the cell is completely sealed during the test, so that none of the gas is discharged by gas leak during experiment. Top and bottom part sections of the cell are supplied with o-rings. The o-rings are replaced at given time intervals to avoid leaks due to wear and tear during mounting / dismounting of the cell.
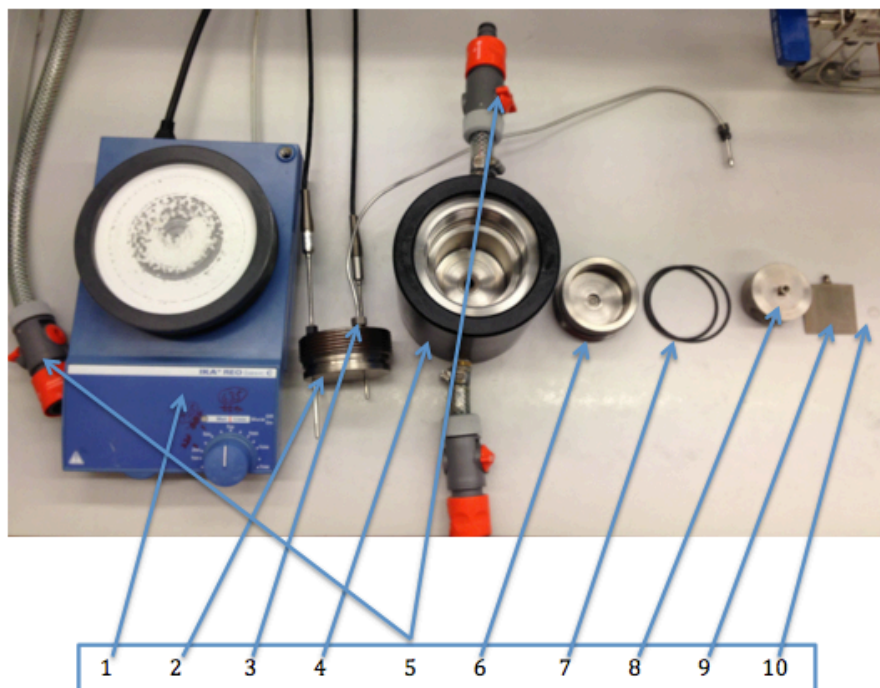
Figure 3.3: The test cell

1. Magnetic stirrer
2. Top lid with two temperature sensors
3. Gas supply
4. Cell house surrounded by water jacket
5. Circulation links for refrigeration circuit
6. Bottom lid
7. O – rings
8. Magnet holder with mounted bearings
9. Stirring blade
10. Nylon ring

Two different test cells, one small and one larger were used. The dimension of the smaller cell (showed in figure 3.2) is 60 mm inner diameter and with a height of 50 mm giving a volume of 141.4 ml. The stirrer blade has a height and width of 45 mm (square shaped) leaving a free space of 7.5 mm between its edges and the cell wall for the temperature sensors. The larger cell has a diameter 90 mm and a height of 50 mm giving a volume of 314.2 ml and the height of the stirrer blade is 45 mm and the width 62 mm leaving a free space of 14 mm between its edges and the cell wall for the temperature sensors. Due to the difference in diameters, similar stirring rates will produce different shear rates and Re-numbers at the cell wall and affect conditions. Thus stirring rate alone cannot be used for comparison of experimental conditions with respect to cell agitation.

3.1.2 The cooling bath and timer

A Julabo F34-HL of the high tech series (left Figure 3.4) has been used to set the desired temperature profiles during an experimental run. The bath has a programmer (see right Figure 3.4) which allows up to 6 different temperature profiles of each up to 60 program steps to be prepared prior to the experiments. The desired profile is activated at start of the run. In the present work pure water has been used as bath fluid for cooling and heating purposes. During experiments the bath is able to maintain stable bath temperature within ± 0.02 °C.

In the experiments done in the present study, the following profiles for the cooling bath has been used:

- Step 0: Stabilization. Bath is left at constant temperature of 13.5 ° C for 10 minutes to stabilize.
- Step 1: Cooling. Cooling down to the experimental temperature over a set time period to produce a desired cooling rate of 3 °C/h.
- Step 2: Remain at the desired temperature until terminated.

Figure 3.4: The cooling bath

When the bath has reached the experimental temperature a 10 minutes dwell time is allowed to stabilize cell temperature before start of the experiment. Start of stirrer is automated by use of a timer that is activated at start of cooling. Activation of the timer shuts off the stirrer power and reconnects power when the timer has completed its time countdown.

3.1.3 Booster

A Resato DBS-160-30-115-D/FU1 gas booster is used to increase the pressure up to a suitable level in the gas container. The capacity of the booster is 800 bar output pressure at an input pressure of minimum 17.5 bar from supply bottle. To maintain pressure at 90 bars during the experiment a YARA CRS-SL 400 pressure reduction valve was used. This valve was mounted at the outlet connection between the gas container and the cell. The valve was able to maintain constant pressure within ± 0.5 bars in the line provided sufficient differential pressure between line and container. Through tests conducted by other personel prior to this thesis it was found that a pressure of 90 bars could be maintained in cell during an experiment provided a container pressure above 150 to 160 bars. Based on this evaluation it was decided to increase pressure in the container to 200 bars at start of experiment.

During experiments the pressure reduction valve was adjusted to 90 bars output line pressure.

3.1.4 Flow meter

The flow meter is a Bronkhorst High-Tech Device. It is a sensor for mass flow and pressure. In this thesis it was used to show the gas flow in the test cell when we made hydrate. The flow meter gives out information in normal millilitre, meaning in atmospheric pressure.

Communication and data exchange between the flow meter and LabView was coordinated by the communication software tool FlowDDE (DDE = Dynamic Data Exchange server, program used to arrange connection between Windows applications such as LabView and digital instruments such as the Bronkhorst flow meter).

During experiments Flow DDE must be set to 'open communication', if not there will be is no connection between LabView and the flow meter.

<p align="center">Figure 3.5: The flow meter.</p>

Prior to specification and purchase of the flow meter, some growth tests were conducted in isochoric cell experiment by other personnel. Based on these tests it was decided to specify an operational range of 0 to 2000 ml/min and the flow cell was requested for use at pressures up to 400 bars while operational pressure for the first experiments was set to 90 bars. Unfortunately the supplier of the instrument made his calibration at 400 bars instead of 90 bars. Thus the meter reading will produce an offset that has to be adjusted for and taken into consideration analyzing the experiments. The flow meter is also calibrated at 20 °C, while the temperature around the flow meter could be as high as 25 to 28 °C due to heat produced by nearby cooling bathes. A Pt-100 temperature sensor was mounted in contact wit flow meter surface for adjustments of the flow meter readings during data analysis (see table 3.1).

Table 3.1: Gas Conversion Factor Calculations

	Fluid from	**Fluid to**
Fluid	CH_4 (Methane)	Air
Flow	2 lm/min (0 °C and 1013.25 hPa)	3.640 ln/min (0 °C and 1013.25 hPa)
Pressure	400 bar	8 bar
Temperature	20 °C	72.1 °C
Density	0.7174 kg/m^3	1.293 kg/m^3
Heat capacity	3342 J/kg K	1019 J/kg K
Viscosity	3.166E-05 Pa s	2.059E-05 Pa s
Thermal cond.	0.08333 W/m K	0.03306 W/m K

3.1.5 Experimental conditions

The experiments have been conducted using two different cylindrical cells, one larger and one smaller (see cap. 3.1.1). The experimental conditions are outlined in Table 3.2. Changes in the volume of water will affect the total amounts of hydrates that can be formed in the cell and the duration of experiment at given conditions. Volume of water in the cells is scaled on basis of level above cell bottom. 50 ml water in the smaller cell and 112.5 ml in the larger cell results in a gas – water interface 18 mm above cell bottom in both cases. Both the temperature and the stirring rate will affect hydrate growth rates. In addition changes in the stirring rate will affect boundary layers at cell wall and heat transfer efficiency. It should be noted that 700 rpm in the smaller cell will result in a water velocity of 2.2 m/s at the cell wall, while 700 rpm in the larger cell corresponds to a water velocity of 3.3 m/s at the wall. At 1200 rpm the velocity of water at the cell wall is 3.8 m/s in the smaller cell. A water velocity of 2.2 m/s at the cell wall could be produced in the large cell reducing the stirrer speed to approx. 470 rpm and a velocity of 3.8 m/s could be produced at a stirrer speed of 810 rpm. Such differences should be taken into consideration comparing experiments conducted in the smaller and the larger cell.

As seen from Table 3.2, in the smallest cell the tests has been done using 50 or 100 ml distilled water (DW), and in the largest cell 112.5 or 225 ml DW was used. The rest of the cells were filled with methane gas with a pressure on 90 bara. The pressure is kept constant at

90 bara throughout the experiment, so when gas is consumed due to hydrate formation gas, gas is continuously added through the flow meter.

Table 3.2: Experiments done:

Cell used	Volume of water	Stirring rate		
		500 RPM	**700 RPM**	**1200 RPM**
Smaller cell	50 ml	8°C, 7°C, 6°C	8°C, 7°C, 6°C	8°C, 7°C, 6°C
	100 ml	8°C, 7°C, 6°C	8°C, 7°C, 6°C	8°C, 7°C, 6°C
Larger cell	112.5 ml		8°C	
	225 ml		8°C	

3.2 Calibration

The Flow meter used during the experiments is recently purchased and had never been used in the hydrate laboratory before. This led to some extra "on site" calibration checkouts before the main experiments could be. The response of the flow meter had to be understood to make accurate corrections during data analysis.

Calibration tests were performed for the flow meter prior to its use for the actual gas hydrate formation experiments. The flow meter was a Bronkhorsk High-Tech Device was supplied with a calibration certificates from the dealer specifying calibration conditions. Method for adjustments to other pressures and temperatures were described in the certificates and needed software (FLUIDAT, 2013) for this operation could be downloaded from the producers web site. The gas flow output values were read and logged by LabView. A conversion factor transformed the LabView output data from liters/min to ml/min. Flow tests were initially conducted to verify correspondence between flow meter output signal and LabView data output. During these tests the cell was mounted and the inlet valve closed. The line pressure was then opened and the line pressure adjusted to 40 bars. The inlet valve on the cell was opened very carefully to allow a controlled flow into the cell. Corresponding flow meter readings and pressure change in cell as function time was used for the signal check. Total amount of gas in cell at the end of each test was calculated based on the real gas equation:

$$PV = znRT \tag{3.1}$$

n = number of moles

P = pressure

R = universal gas constant

T = temperature

V = volume

Z = compressibility factor

Amount of gas added to the cell was calculated from flow meter readings and compared with amounts estimated from the pressure changes in cell during the test. Values were compared for representativeness, and the conversion factor was adjusted in LabView as needed.

3.2.1 Calibration test

The calibration tests were run to determine how the flow meter respond, and to see the difference between the numbers that appears on the computer screen and the real numbers. It was considered the maximum gas flow value.

The tests were conducted in the smaller cell with 50 ml DW, with a constant pressure on 40 bar, a temperature on 17.5 °C and with a stirrer on 500 RPM.

It was conducted six tests to be sure that the result could be trusted. In figure 3.6 we can see one of the test results. From this was the area under the curve calculated and compared with the other tests, to see that we get similar results from all of them.
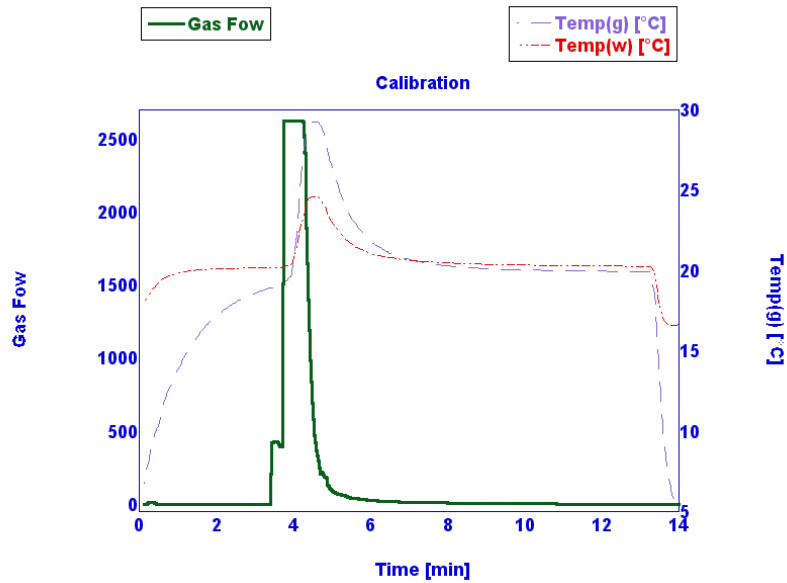
Figure 3.6: A result from one of the calibration tests.

3.2.2 Signal output "recalibration" for 90 bar pressure

From the tests results the maximum flow was 2600 ml/min. From the FLUIDATs website (Table 3.3) and from the calibration certificate (Table 3.4) we find values we can use to calculate the real maximum flow, and then see if there is some difference between this value and the value we got from the tests.

Table 3.3: Data at 100% flow from FLUIDAT website: (FLUIDAT, 2013)

Calibration conditions (methane gas)	
Pressure [bar(g)]	400
Temperature [°C]	20
100% Flow [ln/min]	2
Conversion factor (CF)	1

Equivalent flow air	
Pressure [bar(a)]	8
Temperature [°C]	22.1
100% Flow [ln/min]	3.6
CF	0.5556

Equivalent flow measured (methane gas)	
Pressure [bar(a)]	90
Temperature [°C]	28
100% Flow [ln/min]	2.332
CF	0.8578

Table 3.4: Data from calibration certificate:

Equivalent flow air	
Pressure [bar(a)]	8
Temperature [°C]	22.1
100% Flow [ln/min]	3.704

Table 3.5: Data from lab:

Equivalent flow measured (methane gas)	
Pressure [bar(a)]	90
Temperature [°C]	28
100% Flow [ln/min]	2.621

$$\text{Error} = \frac{100\% \; flow \; air \; from \; calibration \; document - 100\% \; Flow \; air \; from \; FLUID}{100\% \; flow \; air \; from \; calibration \; document} \qquad (3.2)$$

$$\text{Error} = \frac{3.704 - 3.6}{3.704} = 0.028$$

$$\text{Expected value} = \text{Flow measured from FLUIDAT} \cdot \text{Error} + \text{Flow measured from FLUIDAT} \qquad (3.3)$$

$$\text{Expected value} = 2.332 \cdot 0.028 + 2.332 = 2.397$$

The difference between the expected value and the value obteined in the lab:

$$\frac{100 \cdot (100\% \; Flow \; measured \; in \; lab - expected \; value)}{Expected \; value} \qquad (3.4)$$

$$= \frac{100 \cdot (2.621 - 2.397)}{2.397} = 9.32 \ \%$$

This gives a correction factor of: $2000 \cdot (1 - \frac{9.32}{100}) = 1814$

To ensure that the flow readings were with range; the flow results were compared with calculation using the FLUIDAT. It should be noted that the accuracy of the flow meter is within an error margin of 1% for flow rates higher than 20 % of full scale, i.e. 400 ml/min or higher for the given flow meter calibration. For flow rates less than 20% of full scale the accuracy decreases exponentially with decreasing flow rate. The relation between flow rate and accuracy of instrument is illustrated in Figure 3.7.
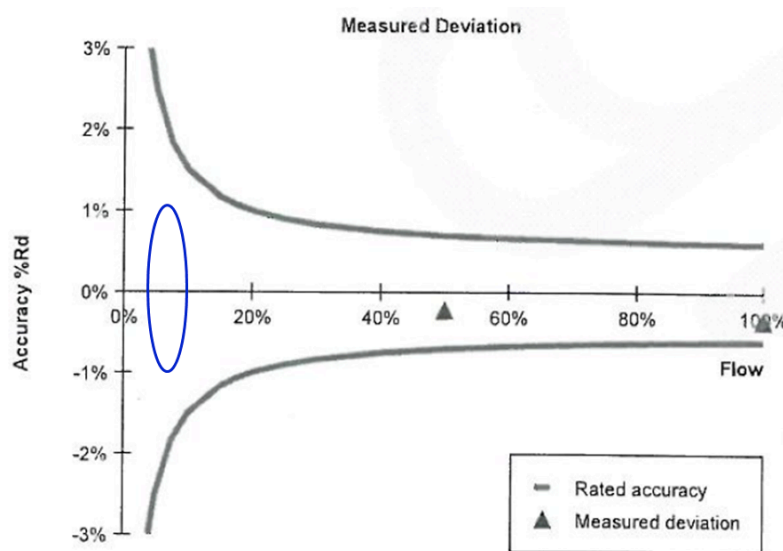
Figure 3.7: Accuracy for the flow meter

The calibration test in Figure 3.6 show a maximum flow reading (cut-off) at 2600 ml/min. According to "recalibration" calculations by FLUIDAT the instrument maximum output level should be 2400 ml/min at 90 bars. In the present work the deviation between the flow logged and the correct value according to the conducted calibration has been accounted for in all analysis of data and corrections have been done.

3.3 Experimental Procedures

The experimental equipment used is described in chapter 3.1.1. The cell assembly is dismounted and the cell is thoroughly washed and rinsed before new experiments. Dismounting and remounting between experiments causes wear and tear and leaks may occur at couplings or over an o-ring sealing. Thus precautions have to be taken and the cell checked for leaks when pressurized and prior to a new experiment. To reduce o-ring wear and tear they are lubricated with a thin film of high vacuum grease before mounting of the cell. Leaks can be detected adding a drop of a dilution of dish washing detergent (Zalo 100) in water on couplings and connections when cell is at experimental pressure prior to start of experiment.

Each experiment is prepared as follows:

3.3.1 Mounting of cell assembly

The magnet holder unit is placed in the magnet house and connected to the stirrer blade axle through the cell bottom. The dead volume between the walls of the magnet house and the magnet holding cylinder is 7 to 8 ml and to avoid residual air being trapped in this unit 15 - 20 ml DW is poured into the bottom magnet housing before mounting of this cell part in the assembly. Water is squeezed into the cell during mounting and the residual air is removed. This water is poured into the sink prior to filling of the cell.

The desired amount of water is then poured into the cell (50, 100, 112.5 or 225 ml) and the top lid is mounted. The top lid connection tubing is connected the inlet valve and the cooling cap is connected the cooling bath via Gardena quick fit connections. The cooling bath is pre adjusted to the desired temperature and the cell is allowed to stabilize around this temperature prior to filling of gas to the cell.

To remove residual air from the cell prior to filling the cell is purged twice with the gas to be used (here pure methane) by filling to 40 bar and discharging to ambient pressure. During this process the cell is stirred for a few minutes (2 – 3 min) at 40 bars to saturate the water with the gas being used and to dilute dissolved atmospheric gases (CO_2, N_2 and O_2) in the water. During gas discharge between purging / filling sequences the stirrer is stopped. When pressure is down to atmospheric the stirrer is run for a few minutes to remove the residues of super saturated gases in the water.

After purging the cell is charged to the desired experimental pressure by exact adjustments of the pressure reduction valve on the gas container. During this process the cell is stirred to saturate the "purged" water with methane gas at the filling conditions (90 bara and 13.5 °C). After filling the cell is allowed to equilibrate for some minutes for the system and temperature to stabilize. When system has stabilized the cooling bath temperature profile selected for the experiment is activated. Activation of cooling bath profile and start of LabView logging is synchronized by simultaneous start-up. The duration of the cooling sequence and the required dwell time before start of stirrer has been pre-programmed on the timer allowing 15 to 30 seconds delay to be synchronized with the temperature profile. Start of timer is coordinated the profile step count down timer on the cooling bath and activated exactly 15 or 30 seconds after the bath dependent on the selected timer delay.

The experiment is now run in an automated mode with start of the stirrer at the desired experimental temperature. Dependent on the experimental temperature and nucleation time, hydrate growth may occur short time after start of stirring or after a nucleation period of some minutes or hours. The nucleation time may affect the level of super-saturation of gas in the water at start of the growth process.

During cooling of the cell it has been observed that the flow meter responds to the cooling by adding smaller amounts of gas to the cell to maintain constant pressure. This shows that the flow meter may respond to volume changes other than gas consumption by hydrate formation and this has to be taken into consideration during analysis of results in case volume changes in the gas due to temperature increases during hydrate formation (exothermic process with energy release) or volume changes of water due to conversion into hydrates.

3.3.2 Parameters recorded by LabView
The LabView datafile contains the following experimental parameters:

1. Logging time in minutes (activation of LabView is zero time)
2. Cell pressure in bara (absolute pressure)
3. Cell temperature in the gaseous phase [°C]
4. Cell temperature in the water phase [°C]
5. Bath temperature [°C]

6. Stirring rate [rpm]

7. Gas flow through flow meter [ml/min]

8. Something missing? Flow meter temperature [°C]

Time interval between loggings was set to 0.05 minutes (i.e. 3 seconds) during all experiments. All instantaneous values of data are showed on the computer screen and selected data can be shown graphically as shown in Figure 3.8. A slight increase of flow from zero level is seen during the cooling section. Onset of hydrate formation and growth is characterized by a sudden increase in gas consumption as shown in Figure 3.8.
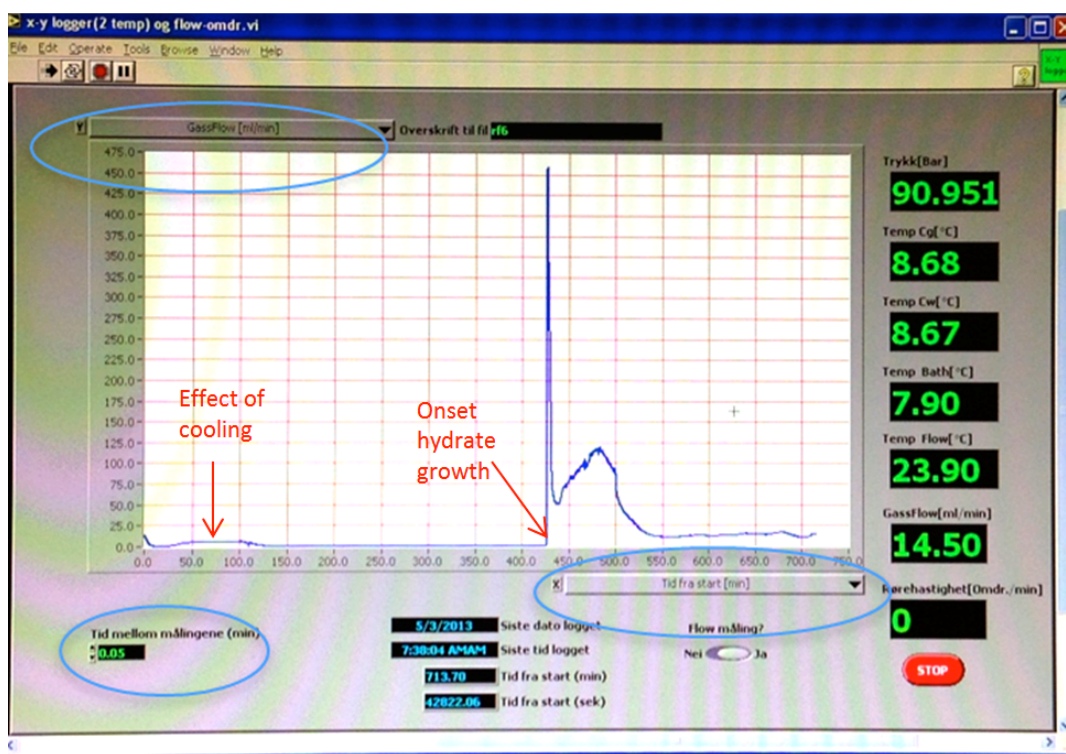
Figure 3.8: LabView with two temperature sensors who is logging every 0.05 s. X-axis represents the time (given in min) and the y-axis represents the gas flow (given in ml/min).

In all the experiments in this thesis, scientific grade 5.5 methane gas supplied by YARA was used (99.9995 % purity). Single component gas is used to avoid effects of gas components being consumed at different rates during hydrate formation. In addition the formation enthalpy and other required properties of methane hydrate can be found in literature.

3.4 Analysis of data

It is assumed that the average hydration number was 6 during experiments, i.e. there are 6 moles of water per mole methane consumed during hydrate formation. Such hydrate number have been reported by several researchers, e.g. Anderson (2004)

3.4.1 Flow and cell temperature response during hydrate growth

Figure 3.9 shows a typical flow – temperature response in cell during hydrate formation. During the first 2 – 3 minutes the growth is increasing rapidly resulting in a flow peak during this period. At the same time the water temperature show a sudden increase as a result of the released heat from the exothermic hydrate formation process. The cell temperature reaches a temperature level that remains fairly stable over a time period indicating that the formation rate proceeds at a relatively stable rate. Also the gas consumption rate drops to a stable level during this period supporting the assumption of constant growth. Towards the end of the growth process growth (through gas flow) and temperature show some increase before both starts marked decrease down towards baseline level. The experiment shown in Figure 3.9 is conducted in the smaller cell at 8 °C bath temperature using 50 ml water and a stirrer rate of 500 rpm. From the point of process start and to the point where the gas flow and water temperature show marked commencing the time lapsed is 30 minutes.
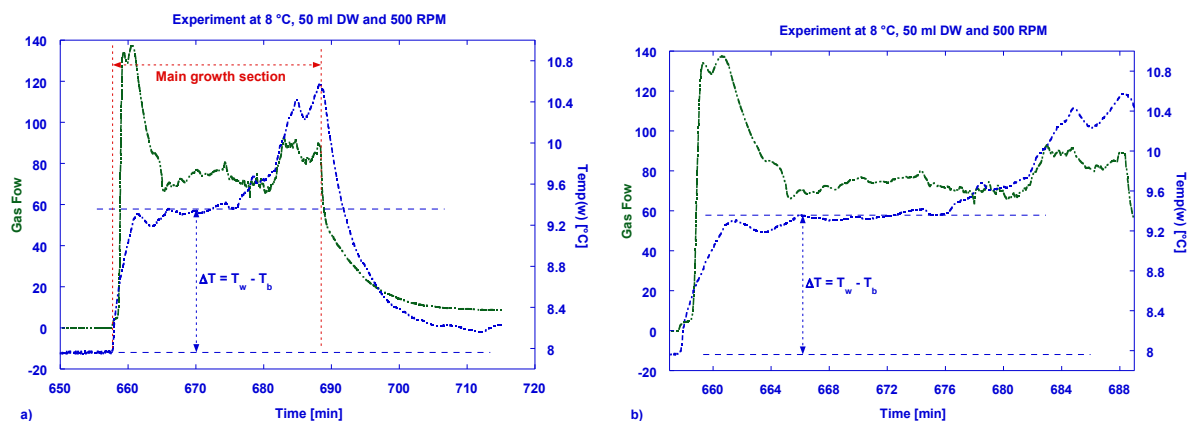
Figure 3.9: Typical flow and temperature responces during hydrate formation and growth in the cell. The figure in a) shows the whole experiment while the main section that can be analyzed is shown in the figure in b).

During growth the water and cell temperature increases and a temperature gradient, ΔT, is established between the interior and exterior (cooling water from the bath). The temperature difference is due to balanced heat production by hydrate formation in the cell and a heat loss

through the cell wall and out in the cooling water. In the present thesis this heat loss is attempted utilized for estimation of the heat production in the cell. A heat loss – heat production model has been established by associate professor Runar Bøe at the Petroleum Department, UiS, and this model is used on the experimental data to examine effects of input heat transfer coefficients and to analyse possible effects of boundary layers (e.g. hydrate slurry at the wall) on the response of the model. The model and simulations are described and discussed later in this chapter.

3.4.2 Gas consumption analysis:

The amount of gas consumed is analysed graphically plotting the measured gas flow into the cell during hydrate growth versus time and calculating the area under the curve, AUC, at each time step, $\Delta t = t_n - t_{n-1}$, during the experiment (see Figure 3.10). AUC is then a sum of trapezoidal regions at each time step and AUC van be calculated according to:

$$AUC = \dot{Q}_{g,n-1} \cdot \Delta t + \tfrac{1}{2}\left(\dot{Q}_{g,n} - \dot{Q}_{g,n-1}\right) \cdot \Delta t \tag{3.5}$$

where $\dot{Q}_{g,m}$ is the measured volumetric gas flow at time step m and Δt is the length of time step. The total amount of gas consumed is given by:

$$AUC_{tot} = \sum_0^t AUC = \sum_0^t \tfrac{1}{2}\left(\dot{Q}_{g,n} + \dot{Q}_{g,n-1}\right) \cdot \Delta t \tag{3.6}$$

where Δt is as described above.
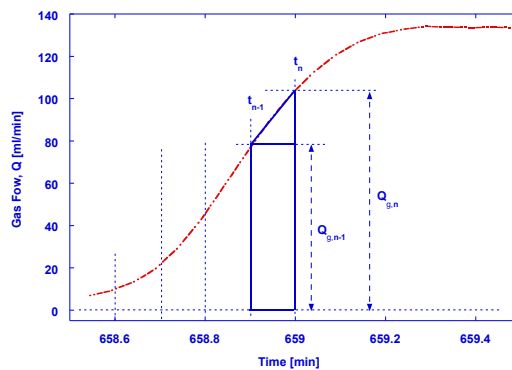
Figure 3.10: Figure illustrating the graphical analysis of the area under the curve, AUC.

47

Given the flow in ml/min and time step in minutes AUC will be given in ml (according to the flow meter output unit). The sum over a given time interval will give the total AUC (AUC_{tot}) and the total amount of gas consumed during this interval. The instantaneous flow value is oscillating around an average and within a section of the experiment the average gas consumption rate (= average gas flow rate) can be calculated by:

$$\dot{Q}_{av} = AUC_{tot}/t_{int} \tag{3.12}$$

where t_{int} is the duration of the time interval for the average.

Figure 3.11 shows AUC_{tot} and the temperature in the water phase as function of time during continuous growth for three parallel experiments. The temperature profiles and growth profiles through AUC_{tot} appears as reproducible within a narrow range. The slope of the AUC_{tot} curve (the derivative of AUC_{tot}) represents the growth rate, and Figure 3.11 indicates decreasing growth rate as function of time from start to end. But within narrow time intervals the growth can be approximated linear relation. This is done in the present work for simplification. Figure 3.11 shows that the growth period can be divided into 3 sections of approximate linear growth. A similar trend was found for all experiments and all parallels independent on cell size, volume of water or stirring rate, but the mentioned parameters could affect the slope of the AUC_{tot} curve within the respective section. The AUC regression curves in Figures 3.12 and 3.14 verify that linearization is ok within sections 1 and 3 (regression coefficient R close to 1), while section 2 shows some deviations from the ideal linearization, but the regression coefficient, R is larger than 0.99 for all of the linear curve fits. The deviation from linearity in section 2 is thus assumed acceptable for the analysis done through the present work. The graphical presentation and regression analysis presented in Figures 3.12, 3.13 and 3.14 are done by use of KaleidaGraph, a software tool specially designed for graphical analysis and presentation.
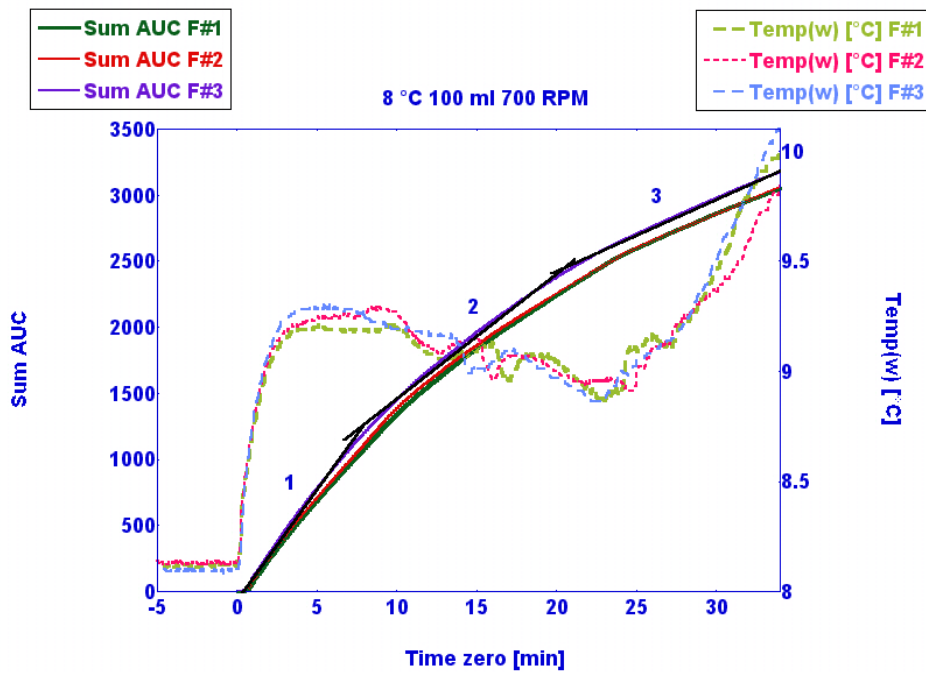
Figure 3.11: Total AUC and temp w vs. time zero. 1 = Initial section, 2 = Mid-section, 3 = end-section

Through the linear curve fit equations as shown in Figures 3.12, 3.13 and 3.14 it is possible to read the linear growth rates within the given section. The linear curve fit equation is given on the form:

$$Y = a + bx \tag{3.13}$$

where Y corresponds to AUC_{tot} in the graph, a is a constant, b is the flow rate in ml / min) and x is the parameter on the x-axis.
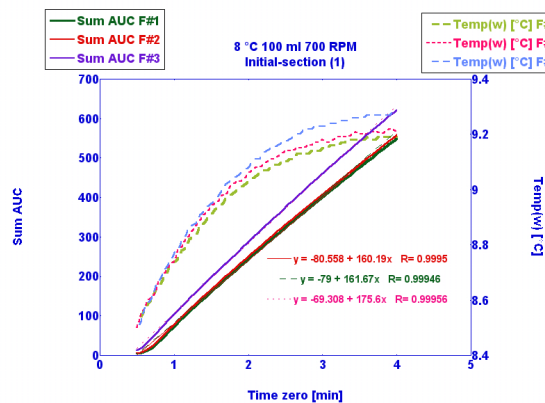
Figure 3.12: Initial section (1)
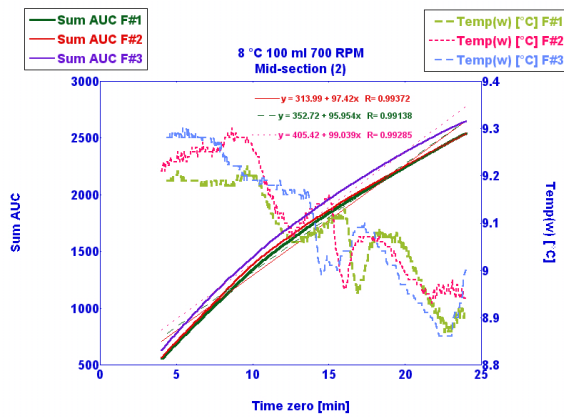
Figure 3.13: Mid-section (2)
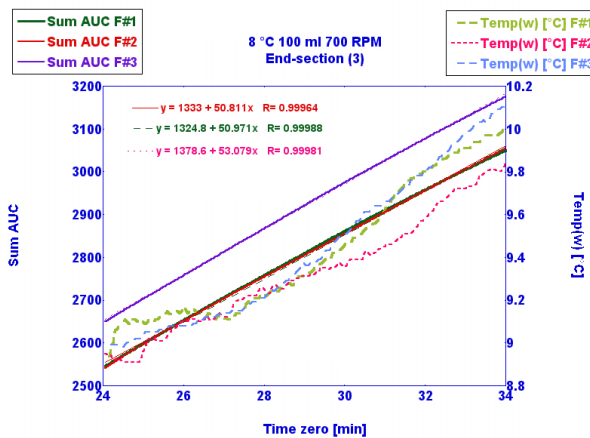
Figure 3.14: End-section (3)

3.4.3 The fractional water conversion into hydrates

When the hydrate start forming in the cell, both the water and the gas are being consumed. The gas consumed is continuously being replaced by frash gas from the container to maintain constant pressure at 90 bars as set by the pressure reduction valve, whereas the conversion of water into hydrate is function of the amount of gas consumed. As mentioned previously we have assumed a hydration number of 6 for all experiments, i.e. each moles of gas consumed corresponds to 6 moles of water consumed. The amount of hydrate formed will affect the properties of the hydrate water slurry and the ability to stir the suspension. At given stage of the process the hydrates may form agglomerates or precipitate on cell surfaces (e.g. stirrer blade, cell wall). Thus information on the fraction of water converted into hydrates during the different stages of the process and the stages analysed is important for evaluation of results. A

hydrate film on the cell wall or precipitates will affect heat transfer. The thermal properties of the hydrate slurry may also be function of the water / hydrate ratio. A water conversion factor can be calculated by:

$$f_w = \frac{n_{w,consumed}}{n_{w,init}}$$
(3.14 a)

where $n_{w,init}$ is the initial amount of water (in moles) present in cell and $n_{w,consumed}$ is the total amount of water consumed at a given stage of the process. Assuming a hydration number of 6 the water conversion factor can be expressed as:

$$f_w = \frac{6 \cdot n_{g,consumed}}{n_{w,init}}$$
(3.14 b)

where $n_{g,consumed}$ is the total amount of gas consumed at a given stage of the process. Multiplying equation (3.14 b) by 100 % we obtain the per cent water converted at a given stage of the process. For the calculations the molar mass of water is set to 18 ($M_{w,H2O} = 18.015$).

3.4.4 Transient heat transfer simulation

Deviations between the enthalpy of formation estimated by the simulation model (read more in Chapter 2.5) and literature data can be due to inaccuracies in the measured experimental data or the estimated heat transfer coefficients at the inner and outer surface of the cell. MatLab was used to edit the simulation program and input was fed directly into the program replacing existing or old values. A printout of the simulator in MatLab is attached in Appendix E.

The heat transfer coefficients used were estimated studying the temperature response of the cell during cooling and heating cycles without hydrate formation. These experiments were conducted by PhD candidate Remi Ermpagano Meindinyos as part of his PhD study. The model was used to simulate temperature profiles and heat transfer coefficients were tuned to fit the measured temperature during the cooling and heating cycles. The best fit heat transfer coefficients were used as input during simulations conducted in the present work. These coefficients did not take into consideration effects of hydrate layers at the interior heat

transfer boundary and discrepancies between simulated formation enthalpies and literature values were thus expected.

We are searching for the unknown heat of reaction, $\dot{q}_R$ (see equation 2.17), and to find this value we must make estimates for the heat transfer coefficient h_i and h_o, at the inside and outside of the cell respectively. It is difficult hard to determine the exact values of these coefficients, especially h_i, because it depends on several factors. It may be reasonable to assume that h_o is greater than h_i. Based on the cooling heating response tests conducted by Remi Ermpagano Meindinyos cooling experiments were used (Meindinyos, 2013) the following heat transfer coefficients were found by tuning simulated temperature response to experimental values:

$h_i = 200$
$h_o = 2600$

These values are based on coarse estimates, but are assumed ok as first stage estimates. Retuning these coefficients could be required.

The flow – temperature response of the experiment to be analysed is plotted and the section of hydrate formation and growth as illustrated in Figure 3.9 b) is identified and selected for analysis. This is done for all parallels of the experimental series. The total gas consumption, AUC_{tot}, is then calculated and presented in an AUC versus time plot to identify growth region 1, 2 and 3 as defined above and illustrated through Figures 3.11, 3.12, 3.13 and 3.14. For the simulations the gas compressibility factor, z, and the heat capacity of the gas are required as input. These are functions of pressure and temperature and were calculated using the software AGA8 from American Gas Association. During the present study the gas pressure was maintained constant at 90 bars and the temperature was varied between 6 and 8 °C. Within this relatively narrow temperature range the compressibility factor and gas heat capacity is fairly constant and we have used average values at all temperatures. By AGA8 the compressibility factor and heat capacity of methane was calculated as:

$z = 0.84$
$c_p = 49$ J/mole*K

In addition the volume of the different phases present of the cell are input parameters to the simulator. Other input values are:

• Cooling water temperature, T_O
• The quantity of gas in the cell at any given time, N_g
• Representative internal temperature, TI_r

Cooling bath temperature is assumed representative for the temperature inside the cooling cap of the cell and is used as input. Ideally the cooling water temperature should be measured at cooling cap inlet and outlet, but the required temperature sensors were not implemented in the set-up used during the present study.

The real gas equation (see equation 3.1) was used for the calculations of the amount of gas present in the gas phase and the amount of gas added via the flow meter. The flow meter provides measured values in normal milliliters per min. Normal milliliter refer to:

1 atm = 1.01325 bar
0 °C = 273.15 K
$z \approx 1$

This gives a conversion factor of 4.46 x 10^{-5} mole/Nml for the gas. The MatLab simulator requires gas consumption in moles and the experimental gas flow data in Nml/min is converted to moles/min and added a new column in the data file. Then AUC is calculated on basis of the gas consumption in moles/min and added new column in the data file and the AUC values are used as input to the MatLab simulator.

The simulation assumes that the entire interior of the cell has a uniform temperature and the representative internal temperature is weighted against the heat content of the individual phases according to:

$$TI_r = \frac{(m_w \cdot c_w \cdot T_w + N_g(t) \cdot cp_g \cdot T_g)}{(m_w \cdot c_w + N_g(t) \cdot cp_g)} \tag{3.15}$$

Since the heat capacity and heat content of water is much greater than the heat capacity and heat content of the gas, the representative internal temperature, TI_r, will be close to the temperature of the water phase.

When temperatures are unknown; we do a transient heat transfer simulation, solving a system of linear equations, once for each time step. For simulations without hydrate generation one assumes that the internal temperature in the cell, TI, will be unknown and resolves with the temperature profile.

When hydrates are formed in the cell, the heat of reaction, q_R, is an unknown factor. q_R can be estimated through the measured TI values. The data for the selected section of the experiment to be analyzed is arranged through an input matrix, equations are solved in a solution matrix and output is sent to an output matrix. In the left hand side of the equation to be solved the heat flow is described through the product of a dimensionless transfer coefficient and an unknown temperature, X_I, while the right hand side generally consists of the product of transfer coefficients, C_I, and known temperatures, T_O^{p+1} (the current outer temperature), T_I^{P+1} (the current inside cell temperature), T_I^P (the start iside cell temperature).

The equation elements of the solution matrix are given on the form:

$$1 \cdot X_I + C_I \cdot T_O^{p+1} = (1 + C_I) \cdot T_I^{P+1} - T_I^P \tag{3.16}$$

where "1" is a dimensionless unit coefficient and the other parameters are as described above. When X_I is determined, the heat generation can be calculated.

Equation (3.16) is derived trough the heat of reaction as given by:

$$q_R = (m_w \cdot c_w + N_g \cdot c_{p,g}) \frac{\partial T}{\partial t} + h_I A_O (T_I - T_O) \tag{3.17}$$

Equation (3.16) is then converted to a discrete heat balance equation according to:

$$q_R = \left(m_w \cdot c_w + N_g \cdot c_{p,g} \right) * \frac{T_I^{p+1} - T_I^p}{\Delta t} + h_I (\pi \delta) 2 r_0 (T_I^{p+1} - T_0^{p+1}) \tag{3.18}$$

Then the discrete heat balance equation is multiplied by $\frac{\Delta t}{(m_w \cdot c_w + N_g \cdot c_{p,g})}$ on both sides and reorganized to:

$$\frac{q_R \Delta t}{(m_w \cdot c_w + N_g \cdot c_{p,g})} + \frac{2h_I(\pi \delta r_0) * \Delta t}{(m_w \cdot c_w + N_g \cdot c_{p,g})} \cdot T_0^{p+1} = \left[1 + \frac{2h_I(\pi \delta r_0) \cdot \Delta t}{(m_w \cdot c_w + N_g \cdot c_{p,g})}\right] \cdot T_I^{p+1} - T_I^p \quad (3.19)$$

Equation (3.16) and (3.19) are of equal physical meaning and then by comparison of the expressions on the left hand side and the right hand side of these equations we see that:

$$X_I = \frac{q_R \Delta t}{(m_w \cdot c_w + N_g \cdot c_{p,g})} \quad (3.20)$$

and

$$C_I = \frac{2h_I(\pi \delta r_0) \cdot \Delta t}{(m_w \cdot c_w + N_g \cdot c_{p,g})} \quad (3.21)$$

X_I, has the dimension "K":

$$[X_I] = \frac{J/_{s} \cdot s}{kg \cdot J/_{kg}K + mol \cdot J/_{mol\,K}} = K \quad (3.22)$$

The simulator use the unit [W=J/s] for the energy. For our purpose we convert to energy flow in J/mole for comparison with literature data on methane hydrate. This is obtained by division of the generated heat from the MatLab simulation with the gas flow into the cell in moles / sec. The heat generated per mole methane consumed is then calculated.

The calculated molar heat generation by methane formation is then compared with literature data. From literature the formation enthalpy of methane is given as 54 kJ/mole methane consumed over a vide range of temperatures (Anderson, 2004).

3.4.5 Examination of the effect of stirring rate on water – gas interface and experimental performance

When the stirrer is started the water is forced towards the cell wall due to centrifugal forces, the water level at the cell wall increases and the water surface obtain a "round edged" conical shape with lowest level at cell centre. The distance between the water surface and the cell wall decreases with increasing height above cell bottom.

To examine the effect of stirring rate on the water surface, some tests were conducted in open cell without the top lid mounted. Tests were conducted in the smaller cell at 500, 700 and 1200 rpm and with 50 and 100 ml water in the cell.

Figures 3.15 and 3.16 show photos of the water surface and the effect of stirring on the water surface in experiments with 50 and 100 ml of water in cell respectively.

Figure 3.15 a, b, c shows the situation with 50 ml of water at 500 RPM, 700 RPM and 1200 RPM respectively. Without stirring the water surface was measured to be 1.5 cm above the cell bottom. At a stirring rate of 500 RPM the level at the cell wall increased to 3 cm above the bottom. At 700 RPM, the water level at the wall reached the top lid inner surface level, and at 1200 RPM some of the water was thrown out of the cell in smaller / larger water droplets.

With 100 ml of water the cell (see Figure 3.16 a, b, c) the water surface reached 3 cm above the bottom in un-stirred cell. 500 RPM force the water surface at the wall up to just above the top lid inner surface level, at 700 RPM to a level above the top lid lower surface, but with fairly smooth water surface and without water being thrown out of the cell. At 1200 RPM, the water splatters in all directions.

This means that the heat transport may be influenced by water wetting the top lid surface at stirring rates above 500 RPM since the top lid is not in contact with the cooling water but the surroundings at room temperature.
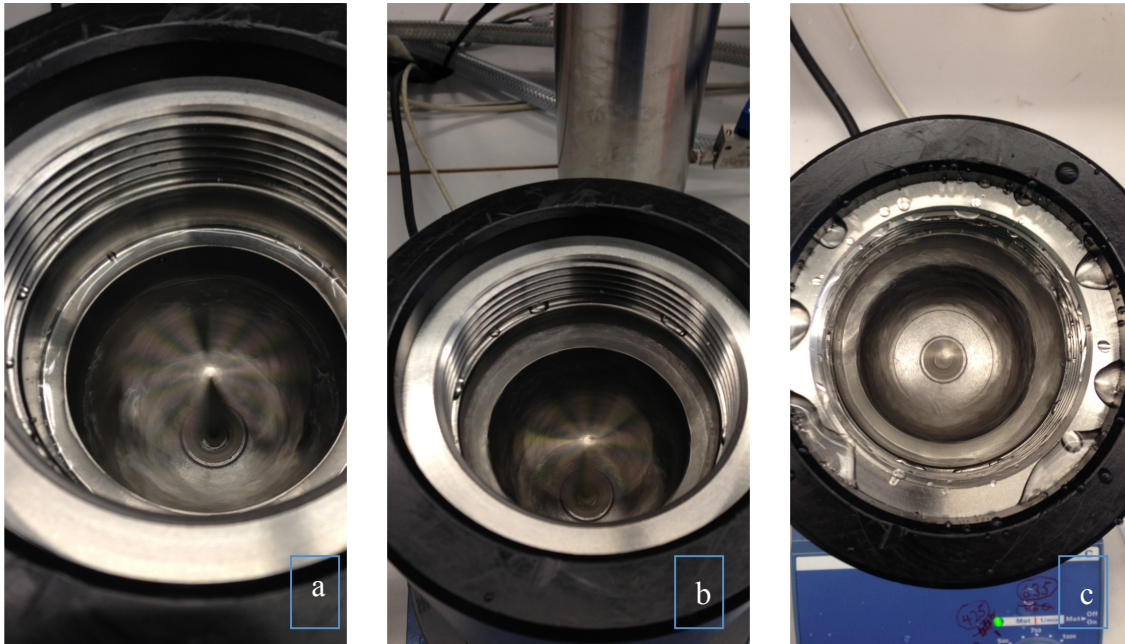
Figure 3.15: Small test cell with 50 ml DW. (a) 500 RPM, (b) 700 RPM, (c) 1200 RPM
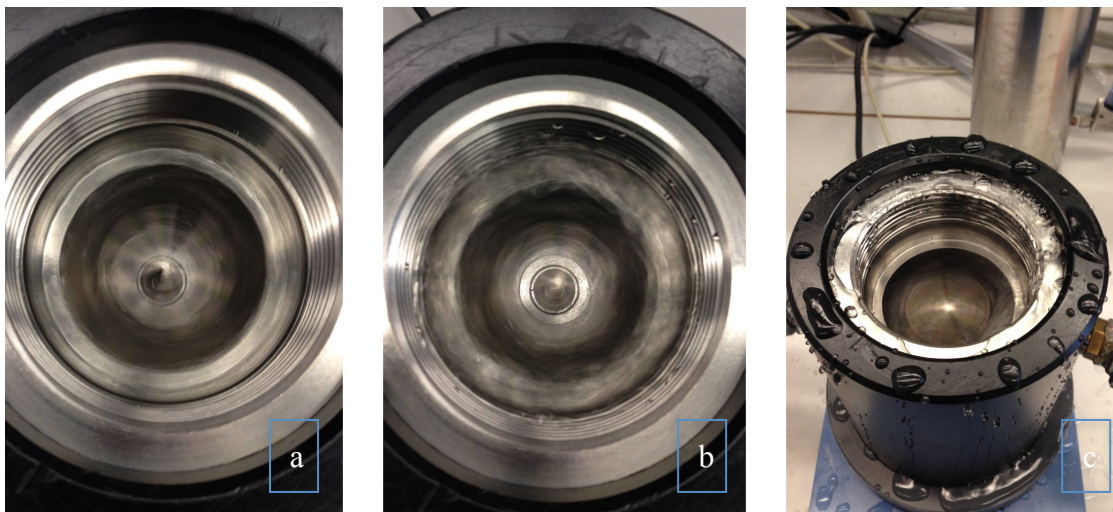
Figure 3.16: Small test cell wit 100 ml DW. (a) 500 RPM, (b) 700 RPM, (c) 1200 RPM.

The amount of water in the cell will also affect the stirring efficiency as function of stirrer speed. The less water we have in the test cell, the less resistance we have on the stirrer, and thus the effect of stirring will most probably not be a simple (linear) function of the stirring rate. The stirring rate will both affect the thickness of boundary layers and at the same time change the fraction of surface being in contact with the water phase. Thus there are two different factors that may affect heat transfer efficiency as function of stirring rate during experiments: a) the thickness and resistance of the boundary layer and b) the contact surface fractional coverage of water.

During all experiments conducted it has been observed that the stirrer meets some temporary increased resistance at some intermediate stages of the process. During this stage the stirrer speed decreases as function of until the decrease stops and the stirrer speed increases back to the original level. The time of occurrence seemed unpredictable, and the effect is believed due to changes in the hydrate water consistency. Figures 3.17, 3.18 and 3.19 shows some effects on the stirring rate during different intervals of the experiment. This phenomenon is taken into consideration during data analysis to evaluate its effect on heat transfer and hydrate growth. There are three different types of stirring problems that are observed to recur during experiments:

1. At some later stage of the hydrate formation process the stirrer speed is observed to drop to zero. This is due to agglomeration and lumps of hydrate blocking the stirrer. This problem did normally occur at a late stage where the formation process was completed and hydrate growth rate approached zero. The region was normally not in conflict with growth region selected for analysis as indicated by Figure 3.17.

2. The stirrer speed gradually decreased towards some minimum level over period of time during the experiment, and then increased back to the pre-set value. This period could interfere with part of the region of growth rate analysis and is illustrated in Figure 3.20. The sudden speed increase could be due to agglomeration and hydrates being pasted on the wall out of contact with the stirrer. A stirring rate above initial level at the end indicates lower resistance against rotation than in hydrate free water at start of experiment (Figure 3.18).

3. The last type is a mixture of the two types listed above. The stirrer speed is stable over a longer period of time before it suddenly drops for a short while and quickly increases to a level slightly above the the initial level. This may indicate some agglomeration and part of the hydrate mass being precipitated on the cell wall. Such precipitation may affect heat transfer and the region should be excluded from region of data analysi (Figure 3.19)
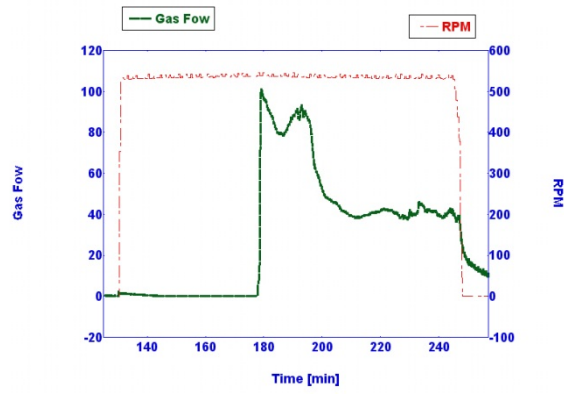
Figure 3.17: Problem with the stirring speed type 1
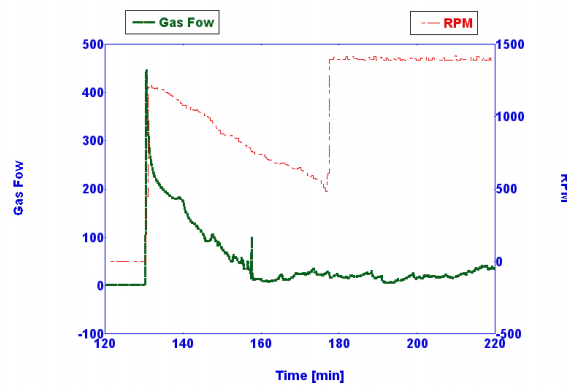
Figure 3.18: Problem with the stirring speed type 2
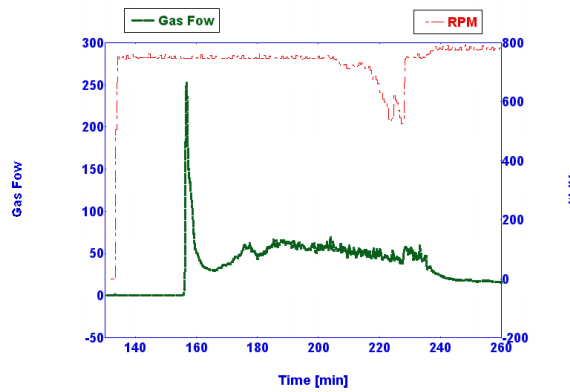
Figure 3.19: Problem with the stirring speed type 3.

By studying the pattern of the magnetic stirrer during the experiments we can avoid including undesired effects in the region analysed.

4 RESULTS

The main results are presented in Figures 4.1 to 4.8 and tables 4.1 to 4.8. Due to the huge amount of experiments conducted and the number of experimental conditions examined these figures and tables present an extraction of main trends and responses as function of system variables such as experimental temperature, stirring rate and the initial amount water present in cell at start of the growth process. Data not presented in this chapter can be found in Appendix A to E.

The amount of water converted into hydrates at end of section for data analysis were estimated to be of the order 15 to 30 % for experiments in the smaller cell and of the order 10 to 33 % for experiments conducted in the larger cell. During one experiment in the smaller cell (at 6 °C, 1200 rpm and 50 ml water in cell) the simulation results showed marked deviation from the other simulations at the same conditions. For this experiment the water conversion was found to be 48.8 % at end of experiment and it was assumed that the result of simulation was affected by agglomeration and deposition of hydrates at the cell wall.

Possible problems due to hydrate agglomeration and deposition is assumed to increase as function of the water conversion ratio, but the results gave indications that the system was able to maintain the hydrates suspended in the water phase for water conversion ratios up to around 30 %. On the other hand simulation problems due to the formation of hydrate slurry boundary layers affecting heat transfer properties is assumed to increase by increasing amount of hydrates present in the cell.

4.1 Gas consumption analysis:

Figure 4.1 shows gas consumption as function of time for experiments conducted in the smaller cell at 8, 7 and 6 °C. With 50 ml water in the cell the initial gas consumption rate (represented by gas flow in the figures) showed a maximum value within the first minute after onset of hydrate formation and growth. Then the gas consumption rate representing a growth rate decreased down to a stable level within the next 2 to 4 minutes. With 100 ml water in the cell the maximum rate was less and decayed more slowly. This comparison showed that the growth path is influenced by the initial amount of water present and the temperature

conditions at start of experiment. The temperature conditions determine a driving force given as a degree of sub-cooling. Since the experiments were conducted at isobaric conditions, the degree of sub-cooling is assumed to give an adequate representation of the driving force.
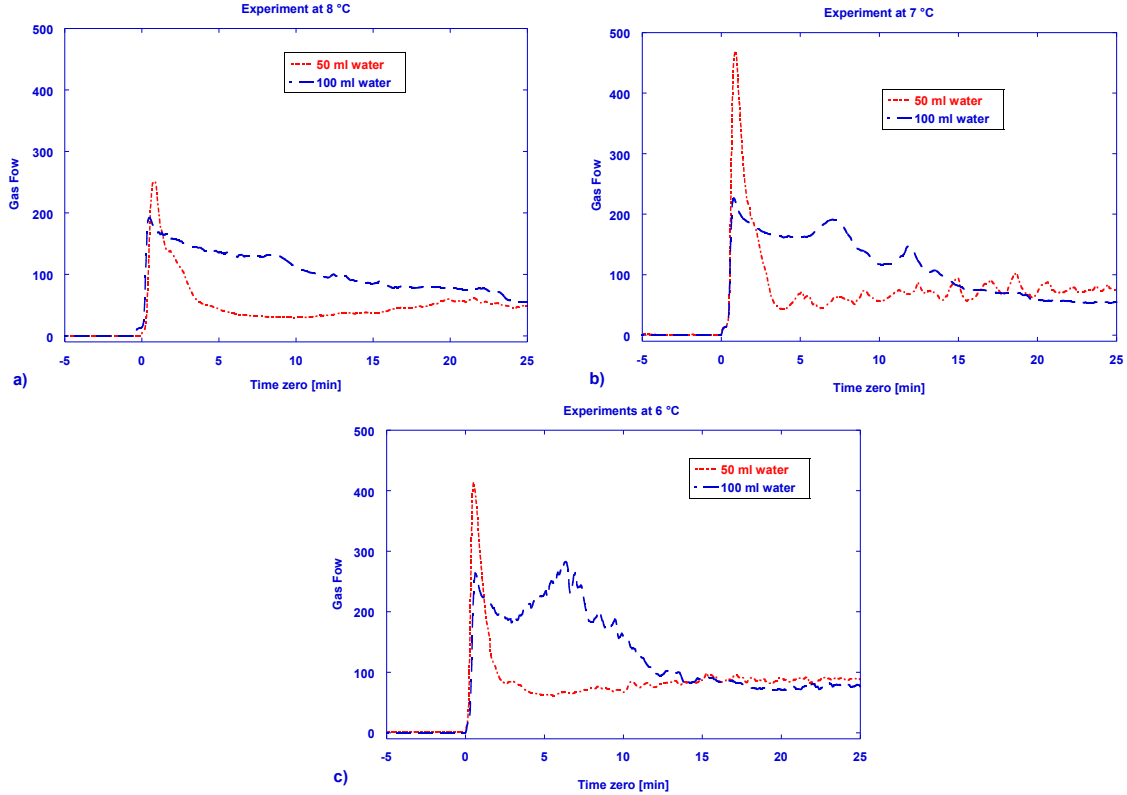
Figure 4.1: Graphs comparing system response during the first 25 minutes of hydrate growth in cell for experiments conducted at 8 (a), 7 (b) and 6 °C (c) and at a stirring rate of 700 rpm.

Table 4.1 shows simulated formation enthalpies during experiments conducted at various conditions. The values in Table 4.1 b) corresponds to simulation over a growth period of 30 minutes shown in Figures 4.1 a), b) and c). For all simulations presented in Tables 4.1 a), b) and c) it is observed that the simulated heat of formation decreases with increasing amount of water present. Literature values for the formation enthalpy of methane hydrate are of the magnitude 54000 J/mole methane consumed over a wide range of temperatures (Anderson 2004). The enthalpies of hydrate formation based on the simulation conducted and as given in Table 4.1 is thus in a range of magnitude that seems reasonable as a first evaluation of the performance of the simulator.

The heat balance of the simulator is described through the equation:

$$\dot{q}_R = \left(m_w \cdot c_w + N_g \cdot c_{p,g} \right) \frac{\partial T}{\partial t} \bigg|_I + h_I \cdot A_0 \cdot (T_I - T_0) \tag{2.17}$$

61

An over-estimated heat of formation may be due to an over-estimated heat transfer coefficient h_I at the boundary layer at the inner cell wall. The input value of h_I is based on examination of heat flow in and out of the cell during cooling and heating cycles without hydrate in cell, just ambient air and water. It is reasonable to assume that the formed hydrates and the hydrate slurry will create additional boundary layer that produce additional resistance against heat transfer. If the correlation between effects of a hydrate slurry boundary layer and heat transfer was simple function of experimental conditions, then the heat transfer coefficient could be tuned to fit the literature formation enthalpy. The values of Table 4.1 are, however, based on calculations over at three growth regions as a whole. The total formation enthalpies as given in Table 4.1 are thus must probably represented by a sum of effects occurring within the individual growth regions, thus the data analysis and experimental performance has to be analyzed further before a final conclusion can be drawn.

Table 4.1: The tables a), b) and c) show simulated average heat of formation at various experimental temperatures at 500, 700 and 1200 rpm respectively. The data input included all three growth regions (1), (2) and (3) as defined in chapter 3.

Expr. conditions	Average ΔH [J/mol]
6 °C 50 ml 500 RPM	74241
6 °C 100 ml 500 RPM	54699
7 °C 50 ml 500 RPM	70522
7 °C 100 ml 500 RPM	62187
8 °C 50 ml 500 RPM	71284
8 °C 100 ml 500 RPM	60535

a)

Expr. conditions	Average ΔH [J/mol]
6 °C 50 ml 700 RPM	72769
6 °C 100 ml 700 RPM	60328
7 °C 50 ml 700 RPM	82564
7 °C 100 ml 700 RPM	53644
8 °C 50 ml 700 RPM	56272
8 °C 100 ml 700 RPM	51077

b)

Expr. conditions	Average ΔH [J/mol]
6 °C 50 ml 1200 RPM	74241
6 °C 100 ml 1200 RPM	54699
7 °C 50 ml 1200 RPM	70522
7 °C 100 ml 1200 RPM	62187
8 °C 50 ml 1200 RPM	71284
8 °C 100 ml 1200 RPM	60535

c)

Table 4.2 shows simulated heat of formation during the control experiments conducted in the larger cell. The trend showing decreased heat of formation by increased water volume as result from simulations is observed, but there is a larger discrepancy between the values and the estimated heat of formation for the experiments with 225 ml water in the cell is far less than the literature value of 54000 J/mole. This can be due to heat transfer calibrations conducted in the smaller cell, effect of size not sufficiently taken into consideration in the

model or other yet un-defined factors. The performance of the larger cell should therefore be investigated further to reveal the un-defined / un-known factors.

Table 4.2: Average heat of reaction measured in the larger cell

Experiment	Average [J/mol]
8 °C 112.5 ml 700 RPM	102798
8 °C 225 ml 700 RPM	37849

4.2 Linear growth rate analysis

Figure 4.2 shows average growth rates measured during experiments in the smaller cell with 100 ml water present. Each of the individual parallels at given experimental condition showed acceptable reproducibility and linear regression coefficients were close to unity. Figure 4.2 a) shows that the initial growth rate (stage 1) increases as function of increasing stirring rate and decreasing temperature (i.e. increasing degree of sub-cooling). This is in accordance with expected and "normal" growth behaviour. During stage 2 the growth rate was lower than during stage 1 and the experiments conducted at 7 and 8 °C show that the growth rate remained relatively stable, but a slight increase as function of increasing stirring rate was noted. At 6 °C showed decreased rate as function of increased stirring the growth rate remained relatively stable at a level above the other two, but a slight decrease as function of increasing stirring rate was noted in contrast to the other two temperatures. The growth behaviour during stage 3 showed similar trends as observed for the 6 °C experiment during stage 2 with decreasing growth rate as function of increased stirring rate. The magnitude of growth rates during stage 3 was above that observed during stage 2 at all stirring rates. Decreasing growth rate as function of increasing stirring rate probably just reflects the simple fact that the process proceeds faster towards the end stage at higher stirring rates and higher driving forces. This may influence the length of experimental section 3 (and probably section 2 in some cases) that can be analysed without complications due to hydrate agglomeration and boundary layer build up.
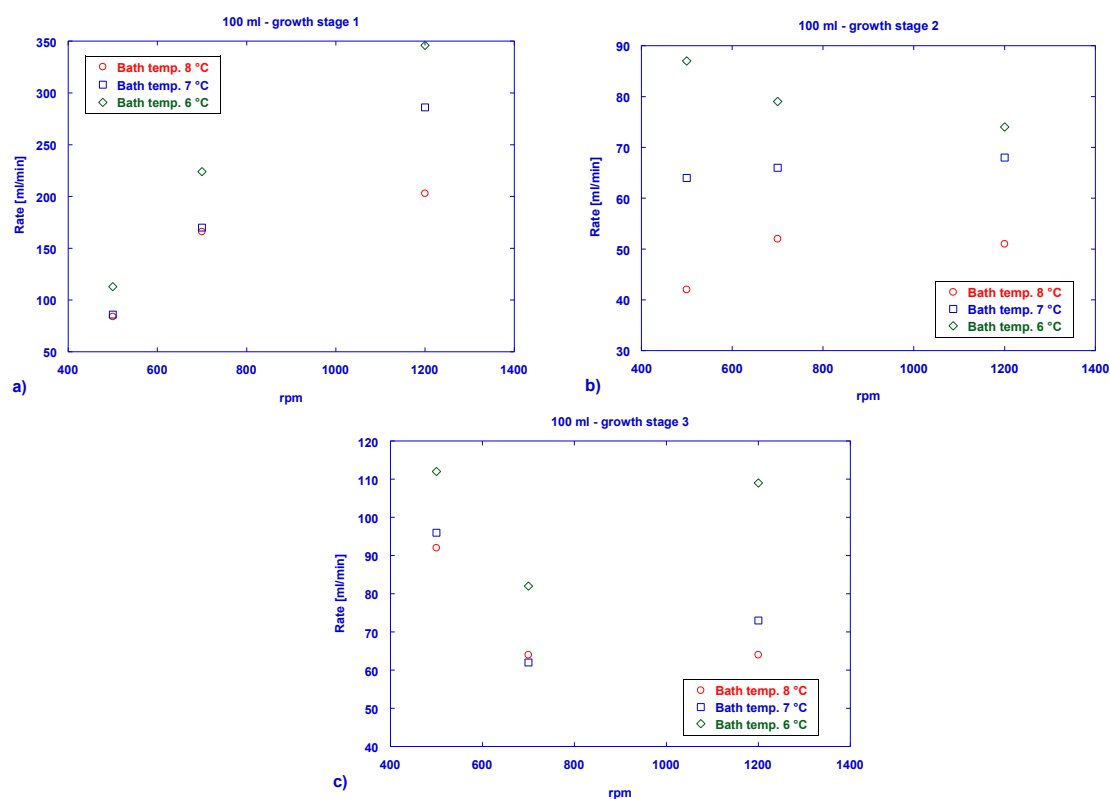
Figure 4.2: Graphs showing linearized average growth rates during growth region 1 (a), region 2 (b) and region 3 (c) as function of stirring rate and experimental bath temperature.

During experiments with 50 ml water the growth rates of stage 1 were higher than those obtained with 100 ml water in the cell while the section 2 rates were lower. This could reflect effects of the water – hydrate ratio and a process that reaches the critical water – hydrate ratio where problems due to e.g. agglomeration at a shorter time period.

4.3 Water converted

Appendix C shows the water conversion ratio (remaining water at end of experiment) for all experiments conducted. Tables 4.3 and 4.4 show the water conversion ratio during the different growth stages of selected, but representative experiments and Figures 4.3 and 4.4 show total gas consumption (given as AUC) and temperature profiles during stage 1, 2 and 3 of the process. During stage 1 the water conversion is low and the influence of formed hydrates on heat transfer can be minimal. However during this period, the cell body will be heated and the temperature profile over the cell wall may not be completely established. In addition the section is of too short duration for separate analysis.

During the mid-section stage 2 of the process the water conversion ratio increases to a level around 10 – 13 % for experiments on 50 ml water. This may be sufficient for boundary layer affected by hydrates to form. In addition heat transfer through the water phase to the cold surface may be affected by the hydrate particles suspended in the water. Heat transfer coefficient h_I would then most probably be overestimated when deduced from the cooling – heating experiments conducted by others (Meindinyo, 2013). The water conversion ratio during stage 2 for the experiments on 100 ml water in the cell was of the same magnitude as the values measured with 50 ml water.

During end stage 3 of experiments with 50 ml water in the cell initially 12 – 25 % of the water is converted into hydrates at end of stage and effects on heat transfer must be assumed. Heat transfer coefficient h_I would most probably be overestimated. The water conversion factor was considerably less for experiments with 100 ml water in the cell and in the region between 12 and 15 %.

Table 4.3: Water converted at 8 °C, 50 ml and 700 RPM

Experiments	Initial-section (1) 0-1.25 min [%]	Mid-section (2) 1.25-19.55 min [%]	End-section (3) 19.55-37.05 min [%]
1	0-1.7	1.7-10.3	10.3-18.3
2	0-2.0	2.0-12.8	12.8-23.3
3	0-1.4	1.4-12.4	12.4-24.5

Table 4.4: Water converted at 8 °C, 100 ml and 700 RPM

Experiments	Initial-section (1) 0-4 min [%]	Mid-section (2) 4-24.05 min [%]	End-section (3) 24.05-34 min [%]
1	0-2.7	2.7-12.3	12.3-14.7
2	0-2.7	2.7-12.2	12.2-14.7
3	0-3.0	3.0-12.8	12.8-15.3
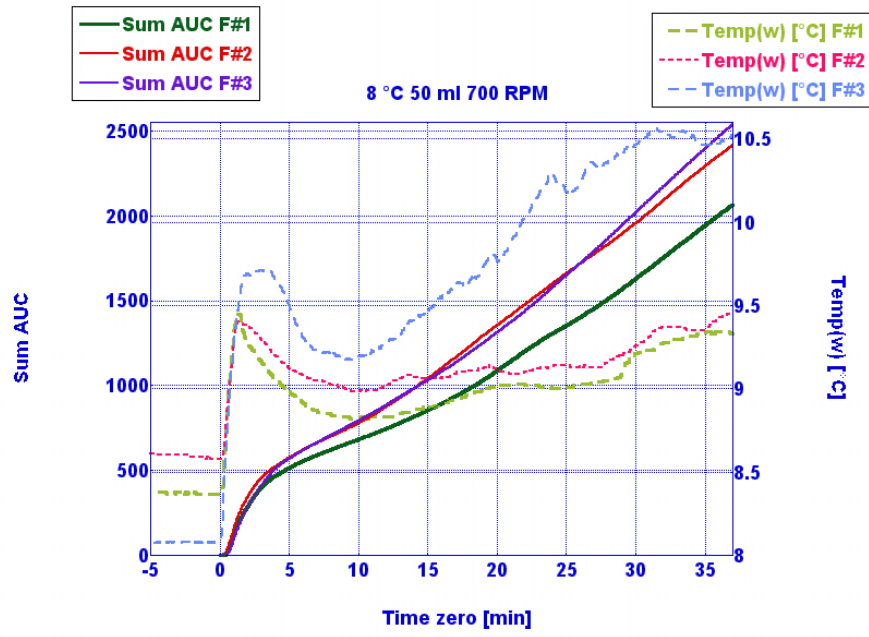
Figure 4.3: Sum AUC vs temp w, 8°C, 50 ml 700 RPM
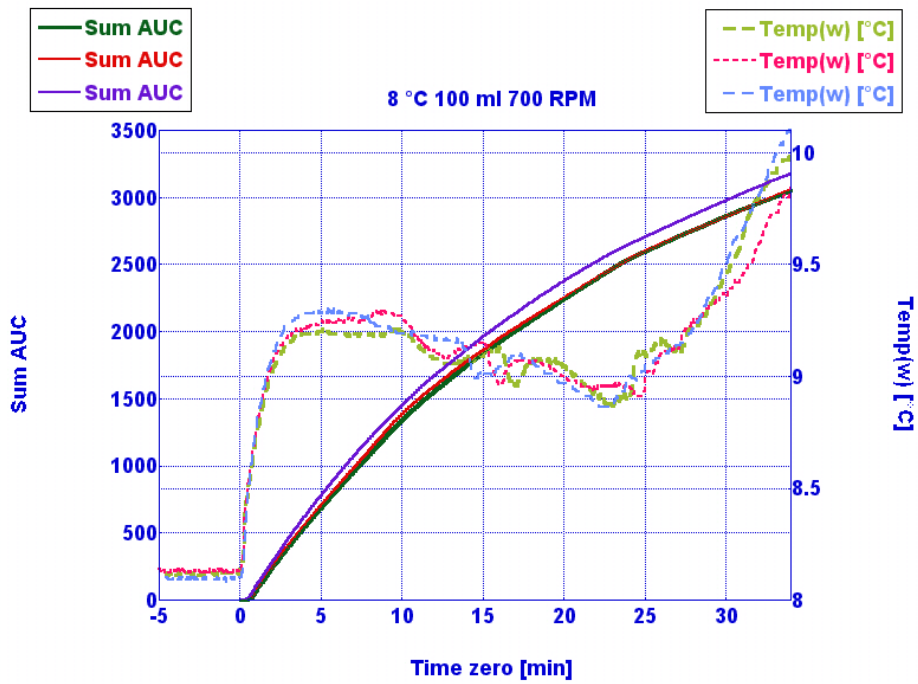
Figure 4.4: Sum AUC vs temp w, 8°C, 100 ml 700 RPM

4.4 Evaluation of transient heat transfer simulation

When we compare all results from simulation (see Appendix D for the whole table), we note that the simulated heat of reaction tends to decrease as the temperature increases. In attempt to find the explanation we first looked at the experiments with 50 ml DW and a stirring rate of 1200 RPM, listed below.

- 6 °C - q_R = 69985
- 7 °C - q_R = 65185
- 8 °C - q_R = 63231

The discrepancy is probably too small to be verified as real effect, but the growth rate and heat release rate will be greater at 6 °C than at the higher temperatures and if heat transport across the wall is over-estimated not taking the effect of hydrate slurry at the boundary layer could be part of the explanation.

Some of the initial simulations showed deviations between parallels outside the "normal" level. These experiments have been re-examined to see if specific effects could have affected the results. For example experiments conducted at 8 °C using 50 ml water and a stirrer rate of 700 RPM and at 8 °C with 100 ml water and 1200 RPM showed greater deviations outside the "normal" trend. Figure 4.5 shows the total gas consumption (AUC) as function of time for the former experiment, while Figure 4.6 shows AUC versus time for the latter experiment. Figure 4.7 shows that parallel 2 and 3 are overlapping up to 25 minutes after onset of hydrate growth, while parallel 1 is displaced towards a lover AUC level. In addition parallel 2 was terminated at an earlier stage of the hydrate formation process than the other two parallels. Initially all simulations on the parallels included the whole part of region 3 included in their data files. The data were then coordinated to cover regions of similar lengths that represented by parallel 2. Table 4.5 compare results from the original simulation and the new simulation based on data interval of same length. The differences between the new and old results were negligible and the recalculation did not give improvement. The difference between parallel 2 and 3 could not be explained, but parallel 1 showed lower growth rate than parallel 3 and this can explain the lower ΔH value by simulation.
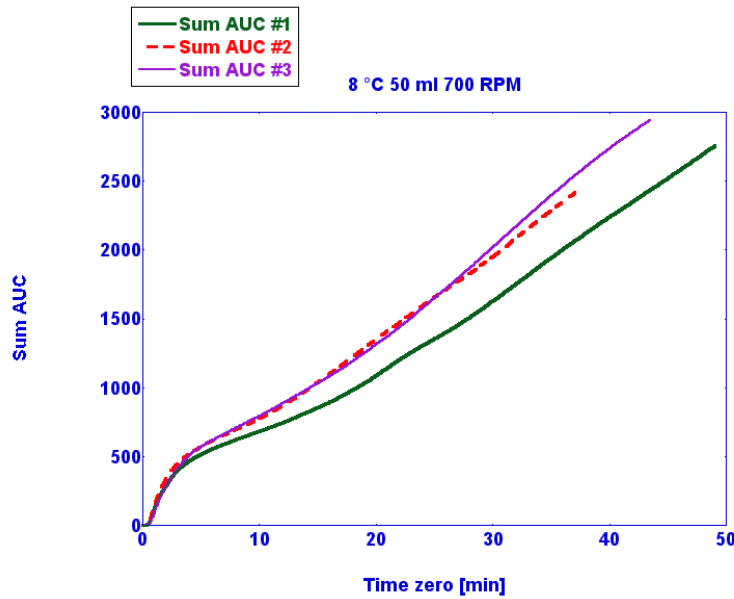
Figure 4.5: Sum AUC vs time zero, 8°C 50 ml 700 RPM

Table 4.5: Old average vs New average on 8 ° C, 50 ml of DW and 700 RPM.

Experiment	Old Average [J/mole]	New Average [J/mole]
Parallel 1	525145	50536
Parallel 2	46084	46084
Parallel 3	70216	68202

For the experiment shown in Figure 4.6 the parallels showed deviating AUC paths towards the end of the growth regions included. Parallel 2 showed deflection on the AUC curve at ca. 18 minutes. It was therefore decided to limit data input for a period of 18 minutes for all 3 parallels and new simulations were conducted to examine effects on the estimated formation enthalpy. The results are given in Table 4.6 and the table shows that the new simulation gave considerably reduced ΔH values, but all three values were of the same region. The heat production is thus under estimated. It is not reasonable to assume heat transfer rate, h_I, greater than the value estimated on pure water system during the cooling – heating experiments. The reason for the deviation must therefore most probably be looked for in other sections of the model. However, one possible explanation could be that the effect is a result the non-steady state condition during stage 1 and loss of produced heat to the cell boby not properly being accounted for by the model.
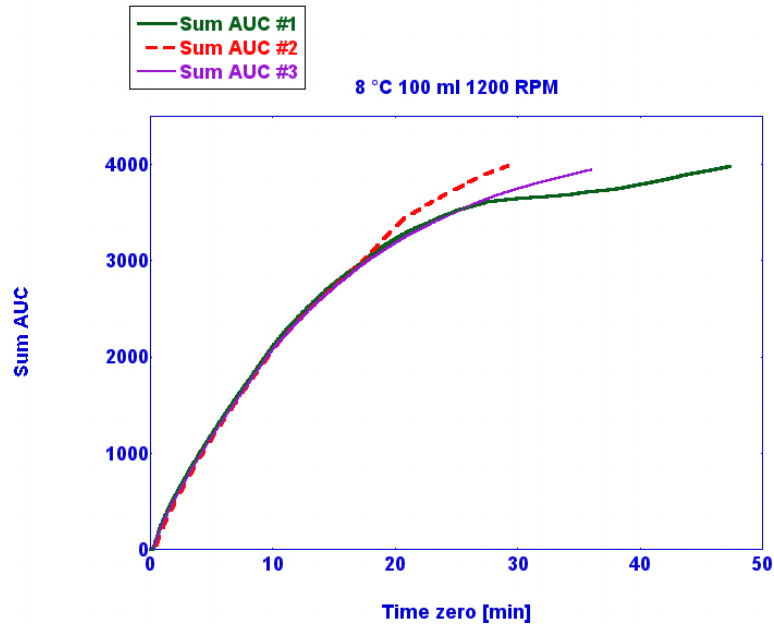
Figure 4.6: Sum AUC vs time zero, 8°C, 100 ml, 1200 RPM

Table 4.6: Old average vs New average on 8 ° C, 100 ml of DW and 1200 RPM.

Experiment	Old Average [J/mole]	New Average [J/mole]
Parallel 1	152678	26047
Parallel 2	46598	24940
Parallel 3	71147	37625

Next we limited the input to data collected during growth phase 2 only. The background for this is that this phase normally shows a stable temperature level meaning that the heat input through hydrate formation and growth balances the heat loss. Then a steady state situation could probably be approached. Figures 4.7 and 4.8 shows AUC and temperature profiles versus time during stage 1 and 2 of experiments conducted at 8 °C and 1200 rpm with 50 and 100 ml water present respectively. For the experiment on 50 ml water region 2 growth could be stated in the time interval between 4 and 20 minutes. For the experiment on 100 ml water region 2 growth was found in the time interval between 3 and 12.5 minutes, but could be prolonged to 17.5 minutes.

The results from the simulations are given in Tables 4.7 and 4.8. These Tables show formation enthalpies far above the literature value and give indications that the heat transfer coefficient, h_I, must be over-estimated. Since this is a region of stable growth and the temperature inside the cell remains relatively stable it could be possible to use this region to

tune the heat transfer coefficient to include boundary layer resistance created by the hydrate slurry. Comparing results in Table 4.7 and 4.8 we see that the simulated formation enthalpies are lower in the experiments with 100 ml water present. The amount of water has effect on the water column and the distance between the gas – water interface ant the cell wall over the height of the cell chamber. This could affect the heat transport in system and should probably be considered to improve the model description of the system. Care should be taken if region 2 simulations are used to tune heat transfer coefficient, but such tuning could be informative if handled with "care" not to over-estimate the effect of boundary layer and not taking other possible effects into consideration.
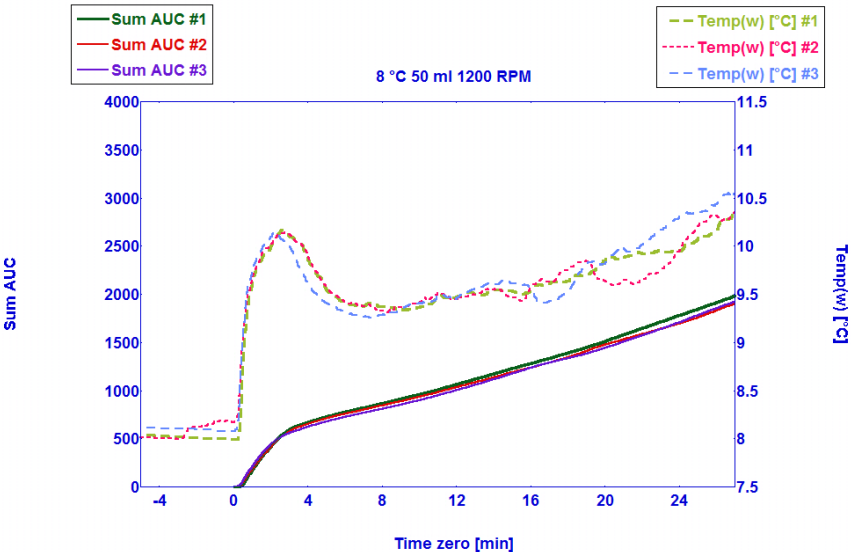
Figure 4.7: Sum AUC vs temp w, 8°C, 50 ml, 1200 RPM
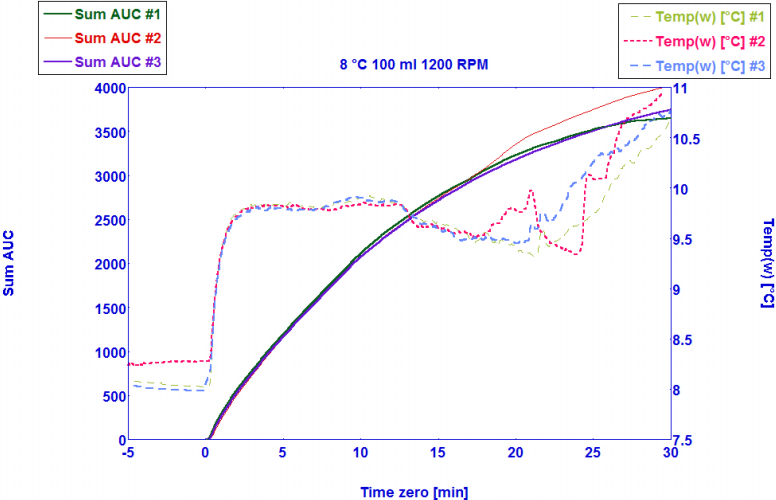
Figure 4.8: Sum AUC vs temp w, 8°C, 100 ml, 1200 RPM

71

Table 4.7: Experoments on 8 ° C, 50 ml of DW and 1200 RPM.

Experiment	Average 4-20 min [J/mole]
Parallel 1	269223
Parallel 2	275134
Parallel 3	270843

Table 4.8: Experoments on 8 ° C, 100 ml of DW and 1200 RPM.

Experiment	Average 3-12.5 min [J/mole]	Average 3-17.5 min [J/mole]
Parallel 1	97188	109170
Parallel 2	95129	103381
Parallel 3	97975	107965

5 UNCERTAINTIES

When an experiment is run, there will always occur some uncertainties due to effects from equipment and experimental method not being accounted for initially. We have two different types of uncertainty that are important to take into consideration, systematic uncertainty and random uncertainty.

Systematic uncertainty is uncertainty due to instruments and method. Since the method has been under development and examination during the present work and the fact that we can't see inside the cell and confirm the quality of the hydrate slurry or state agglomeration there will be lacks of information for the evaluation of results.

Uncertainties in measured temperature and pressure are assumed low using high precision sensors of high quality. Temperature sensors have an accuracy of ± 0.1 ° C and the pressure sensor has an accuracy of ± 0.25 bar.

One of the major uncertainties is connected to the flow meter due to its calibration range versus the main flow range experienced during the experiments. The flow meter was requested calibrated to cover the range up to 2000 Nml/min. Information on the calibration certificate states exponentially increasing inaccuracy in meter readings at flows less than 20 % of full scale, i.e. flow rates less than 400 Nml/min. During most experiments stable level flow rates were less than 100 to 150 Nml/min thus outside the high precision range of the instrument. Based on the experience gained through the present study recalibration of the instrument is planned.

The second major uncertainty is the thermal coefficient, h_I and h_o. Only these two factors have been considered and evaluated during data analysis. Instrument accuracy was not considered and the examination of results were focused on trends to understand the system rater than accurate measurements.

6 CONCLUSION

A large number of experiments have been conducted to evaluate experimental performance at various conditions versus simulations. A model attempting to relate hydrate growth rates to heat transfer in system have been examined. Experiments have been conducted in two different cells of similar geometry but of different sizes. Average growth rates have been presented as AUC.

Experiments conducted in the smaller cell with 50 ml water present always gave a higher formation enthalpy through the simulations as compared to experiments with 100 ml water in the cell except for the two experiments conducted at 8 °C and 1200 rpm, where the highest formation enthalpy by simulation was found for the system with 100 ml water. A reasonable explanation for this deviation cannot be given due to the limited number of parallels run.

From the simulation results there is a clear trend showing that the calculated formation enthalpy decreases when the volume of water in the cell increases and when the stirring speed in increases. This may be due to variations in the boundary layer and effects thereof and should be examined further.

There is reasonably consistency between the parallels that are running by the same conditions, and the small differences that occur are within a range acceptable for the type of experiments conducted.

All experiments showed growth rate behavior that could be divided into three sections

- Initial-rate (1)
- Mid-Section (2)
- End-section (3)

The initial stage (1) is of short duration and is an un-steady state condition represented by a sudden phase transition and release of larger amount of energy stored in a super-cooled and meta-stable system.

The results from the analysis of stage (2) region shows that the temperature gradient across the cell is relatively constant, and may represent an ideal area for analysis. When we analyzed this area we saw that the calculated values of given conditions was very close within a small distribution range, but the enthalpy was very high. Simulations of region 2 can perhaps be used to tune the heat transfer coefficient to include the effect of hydrate slurry in the boundary layer.

Because of the high formation enthalpy values we obtained, we can say that the thermal coefficient, h_I and h_O, is most probably overestimated.

The flow meter should be recalibrated so that the meter range is better fitted to the actual flow level to increase accuracy and reduce measurement uncertainty. One suggestion is to use two flow meters that are connected in series, where one is calibrated to higher values experienced in the initial flow peak and the other is calibrated to lower values of a range representative for the stable growth sections (2) and (3). Accurate measurements during stage (2) and (3) are more important than during stage (1). Secondly as indicated by the varying experimental conditions tested the simulation model based on ideality which differs from the experimental conditions and there may be room for improvement that better takes experimental effects into account.

7 FUTURE WORK

Based on the results from this thesis I have found the answers to several, but not all, of the questions that came into my mind during the work. This has created new questions to which I should be considered. One semester of MSc thesis work is much too short to find all answers, so I will briefly summarize some recommendations for further work below.

Firstly the thermal coefficient, h_i and h_o should be examined further for better fit. Based on the results from the present thesis it seems that the coefficients are over-estimated. The estimation of these coefficients was based on an outer temperature measured in the cooling bath and not on the inlet and outlet of the cooling cap. Introduction of temperature sensors in this section will most probably give some improvement in the estimation of reliable, initial heat transfer coeficients. I would therefore try to revise down the values slightly. Maybe first just take down h_I, then the h_O and then both and then compare all these results together with the results of this task and earlier studies. Based on this, could we come up with some exact coefficients which in turn would lead to accurate results.

As previously mentioned, more than 3-4 parallels should have been included per set of experimental conditions, around 5 to 6 parallels in minimum until experimental effects are better understood and the model is verified to give predictions of acceptable accuracy.

Lars Jensen, in his doctoral dissertation (Jensen, 2011) made some growth rates measurements of methane at 56 bar and 4 ° C (t_{eq} = 7.6 ° C) at 450 rpm in a cell smaller than that used in the present study (66.5 ml total volume and 15 ml of distilled water added). At these conditions he obtained a linear relationship between growth versus time. His experiments were conducted at a lower driving force than used during the present work. Lower driving force would give slower growth rates and probably allow analyses over a wider time span than allowed for during the present work. So I would propose that some experiments where the results can be compared to the effect of force on the kinetic reaction should be done. The temperature used in his PhD thesis corresponds to an experimental temperature of 8.4 ° C at 90 bars. In the smaller cell experiments at 8 °C and 90 bars often resulted in a long nucleation period and to cut down the duration of the experiment and be

able to conduct a greater number of experiments 8 °C was set as maximum temperature for the experiments. In the larger cell nucleation occurs more readily and in this cell the experimental temperature could be increased to approximately 10 °C according to a parallel BSc study on methane hydrate nucleation during the semester (BSc candidate Daranphop Hongbua, UiS, 2013). During the present study only limited experiments could be conducted in the larger cell since this was mainly occupied by another student. Experiments at lower driving force are possible in the larger cell, but the experimental growth performance for this cell is not yet well examined and would require series of new experiments. This cell could also be run at similar conditions as used by Lars Jensen to verify that growth behaviour is fairly reproducible.

Lars Jensen's PhD used water conversion to quantify the amount of hydrates formed while the present work has used "sum AUC", which easily can be converted to water conversion. AUC represents a "global" growth rate and is not related to the number of hydrate particles and their surface area where the real growth process takes place. A representation by the amount of water converted could be a better measure of growth conditions in comparison between growth behavior in equipment of different sizes.

It could also be interesting to examine growth in systems containing anti agglomerants to ensure that agglomeration and precipitation on equipment surfaces are minimized. Such chemicals could affect growth rates in an un-desired direction, but can be worth some trials.

To obtain better and more reliable results from new tests I will recommend (if possible) using two flow meters in series, instead of one. One of the flow meters should be calibrated to cover the initial flow peak, the other the flow range experienced during the main growth period. Also additional temperature sensors at the cooling cap inlet and outlet will improve the data quality. For better examination of heat transfer through the cell wall, temperature sensors in direct contact with the outer and inner wall surfaces in addition to one in the body of the wall could be optimal. But the implementation of such sensors will be difficult due to the present construction of the cells.

References

Abay, H.K. and T.M. Svartaas, *Multicomponent Gas Hydrate Nucleation: The Effect of the Cooling Rate and Composition*. Energy & Fuels, 2010

Anderson Graydon K., *Enthalpy of dissociation and hydration number of methane hydrate from the Clapeyron equation*. 2004, Los Alamos National Laboratory, Los Alamos, US

Arjmandi, M., B. Tohidi, A. Danesh, and A.C. Todd, *Is subcooling the right driving force for testing low-dosage hydrate inhibitors?* Chemical Engineering Science, 2005.

Balson, T. *Chemistry in the oil industry VII: performance in a challenging environment*. in *International Symposium on Chemistry in the Oil, Industry*. 2002. London: The Society.

Bergeron Sebastien, Beltrán Juan G., Servio Phillip, *Reaction rate constant of methane clathrate formation*. 2010, Department of Chemical Engineering, McGill University, Canada

Bo-Hui Shia, Jing Gonga, Chang-Yu Sunb, Jian-Kui Zhaoa, Yao Dinga, Guang-Jin Chen, *An inward and outward natural gas hydrates growth shell model considering intrinsic kinetics, mass and heat transfer*. 2011 by Elsevier B.V. China

Buanes, T., Kvamme, B., Svandal, A., *J. Cryst. Growth*, **287**, 491 (2006).

Carroll John, *Natural Gas Hydrates; A Guide for Engineers, Second Edition*, Elsevier 2009 USA

Carroll J., *Natural gas hydrates- A guide for engineers*. 2003 by Gulf Professional Publishing

Christiansen Richard L. and Sloan Dendy E. JR, *Mechanisms and Kinetics of Hydrate Formation*. 1994, Colorado

Christiansen R.L., Sloan E.D., *Proc. First International Conference on Natural Gas Hydrates*. 1994, New York Academy of Sciences

Davies Simon R., Boxall John A., Dieker Laura E., Sum Amadeu K., Koh Carolyn A., Sloan E. Dendy, Creek Jefferson L., Xu Zheng-Gang, *Predicting hydrate plug formation in oil-dominated flowlines*. 2010 by Journal of Petroleum Science and Engineering. USA and Norway

Davy, H. Philosophical Transactions. Ser. B **1811**, 101, 1.

Del Villano, L. and M.A. Kelland, *An investigation into the laboratory method for the evaluation of the performance of kinetic hydrate inhibitors using superheated gas hydrates*. Chemical Engineering Science, 2011.

Englezos, P., Kalogerakis, N., Dholabhai, P.D., Bishnoi, P.R., *Chem. Eng. Sci.*, **42**, 2647, (1987a).

Englezos, P., Kalogerakis, N., Dholabhai, P.D., Bishnoi, P.R., *Chem. Eng. Sci.*, **42**, 2659, (1987b).

Eugene A. Smelik and H. E. King, *American Mineralogist, February 1997, v. 82, p. 88- 98*

Freer, E., Selim, M.S., Sloan, E.D., *Fluid Phase Equilib.*, **185**, 65 (2001).

Fukumoto, K., Tobe, J.-I., Ohmura, R., Mori, Y.H., *AIChE J.*, **47**, 1899, (2001).

Hammerschmidt, E. G. *Ind. Eng. Chem.* **1934**, *26*, 851.

He Yuanyuan, Rudolph E. Susanne J., Zitha Pacelli.L.J., Golombok Michael, *Kinetics of CO$_2$ and methane hydrate formation: An experimental analysis in the bulk phase*. 2011, Delft University of Technology, The Netherlands

Heriot Watt University, homepage, Edinburgh.

Hirai, S., Tabe, Y., Kamijo, S., Okazaki, K., *Therm. Sci. Eng.*, **8**, 1, (2000).

Hirai, S., Sanda, H. , *Am. Mineral.*, **89**, 1260, (2004).

Hongbua Daranphop, BSc candidate, UiS, 2013, Stavanger

Incropera F.P., DeWitt D.P., *Fundamentals of heat and mass transfer*, 2end Ed. 1985, John Wiley & Sons

Ito, Y., Kamakura, R., Obi, S., Mori, Y., *Chem. Eng. Sci*, **58**, 107 (2003).

James J. De Yoreo, Peter G. Vekilov, *Principles of Crystal Nucleation and Growth*. 2003 USA

Jensen Lars, Ph.D. Thesis 2011, *Experimental investigation and molecular simulation of gas hydrates*. *DTU Chemical Engineering*, Danmark

Jinping Li, Kaihua Guo, Deqing Liang and Ruzhu Wang,*Experiments on fast nucleation and growth of HCF141b gas hydrate in static water columns*. 2004 by Elsevier

Kato, M., Iida, T., Mori, Y.H., *J. Fluid Mechanics*, **414**, 367 (2000).

Kvenvolden, K. A.; McMenamin, M. A. *Geol. Surv. Circ. (U.S.)* **1980**, *825*, 1.

Kvenvolden, K. A.; Ginsburg, G. D.; Soloviev, V. A. *Geo-Marine Letters* **1993**, *13*, 32.

Kvenvolden, K. A.; Golan-Bac, M.; McDonald, T. J.; Pfaum, R. C.; Brooks, J. M. *Hydrocarbon Gases in Sediment of the Voring Plateau, Norwegian Sea*, US Geological   Survey, Texas A&M Univ., 1989.

Kelland, M. A. *Energy & Fuels* **2006**, *20*, 825.

Kashchiev, D.; Firoozabadi, A. *J. Crystal Growth* **2002**, *243*, 476.

Kashchiev D., Firoozabadi A., *Nucleation of gas hydrates*. 2002 by Elsevier, Bulgaria and USA.

Kelland M.A., *Production Chemicals for the Oil and Gas Industry*. 2009 by Taylor & Francis Group. Florida

Larson M.A., Garside J., *Chem. Eng. Sci*, 1989, Elsevier

Lievois J.S., Developmen of an Automated, High Pressure Heat Flux Calorimeter and Its Application to Measure the Heat of Dissociation of Methane Hydrate, Ph.D. Thesis 1987, Rice University

Maini, B.B., Bishnoi, P.R., *Chem. Eng. Sci.*, **36**, 183, (1981).

Makogon, Y., Makogon, T., Holditch, S., in *Proc. Japan National Oil Conference*, 259,Tokyo, (1998).

Makogon, Y. F.; Trebin, F. A.; Trofimuk, A. A.; Tsarev, V. P.; Chersky, N. V. *Dokl. Akad. Nauk, SSSR* **1971**, *196*, 203.

Makogon, Y. F, *Gazov. Promst.,* 1965, 5, p14.

Malegaonkar, M.B., Dholabhai, P.D., Bishnoi, P.R., *Can. J. Chem. Eng.*, **75**, 1090 (1997).

Meindinyo Remi E., Ph.D. student, UIS, 2013, Stavanger

Mochizuki, T., Mori, Y.H., *J. Cryst. Growth*, **290**, 642 (2006).

Mochizuki, T., Mori, Y.H., In *Proc. Fifth International Conference on Gas Hydrates*, Trondheim, Norway, June 13–16, Paper 1009 (2005).

Mori, Y.H., *J. Cryst. Growth*, **223**, 206, (2001).

Mosayyeb Arjmandi, Bahman Tohidi, Ali Danesh, Adrian C. Todd. *Is subcooling the right driving force for testing low-dosage hydrate inhibitors?*. 2004 by Chemical Engineering Science

Moudrakovski, I.L., McLaurin, G.E., Ratcliffe, C.I., Ripmeester, J.A., *J. Phys. Chem. B*, **108**, 17591, (2004).

Mullin, J. W. *Crystallization*; Butterworth-Heinemann: Oxford, 1993; Vol. 3.

Nojima, K., Mori, Y.H., in *Proc. Tenth International Heat Transfer Conference* (Hewitt, G.F., ed.) Brighton, UK, **3**, 377 (1994).

Ohmura, R., Kashiwazaki, S., Mori, Y.H., *J. Cryst. Growth*, **218**, 372 (2000).

Ohmura, R., Ogawa, M., Yasuka, K., Mori, Y.J., *J. Phys. Chem. B*, **107**, 5289 (2003).

Ripmeester, J. A.; Tse, J. S.; Ratcliffe, C. I.; Powell, B. M. *Nature* **1987**, *325*, 135.

Rowley J.L., *Statistical Mechanics for Thermophysical Property Calculations*. *1994, Prentice Hall Inc*

Sabase Yuichiro and Nagashima Kazushige, *Growth Mode Transition of Tetrahydrofuran Clathrate Hydrates in the Guest/Host Concentration Boundary Layer*. 2009 by Meiji UniVersity. Japan

Salamatin, A.N., Hondoh, T., Uchida, T., Lipenkov,V.Y., *J. Cryst. Growth*, **193**, 197, (1998).

Servio, P., Englezos, P., *Crystl. Growth Design*, **3**, 61 (2003).

Shindo, Y., Lund, P.C., Fujioka, Y., Komiyama, H., *Int. J. Chemical Kinetics*, **25**, 777, (1993).

Skovborg, P., Rasmussen, P., *Chem. Eng. Sci.*, **49**, 1131 (1994).

Sloan E.D. and Koh, C.A., *Clathrate Hydrates of Natural Gases – Third Edition*, 2008 by Taylor & Francis Group, LLC. Florida

Smith, J.M., H.C. Van Ness, and M.M. Abbott, *Introduction to chemical engineering thermodynamics*. 2005, McGraw-Hill

Sugaya, M., Mori, Y.H., *Chem. Eng. Sci.*, **51**, 3505 (1996).

Sum Amadeu K., Koh Carolyn A., and Sloan E. Dendy, *Developing a Comprehensive Understanding and Model of Hydrate in Multiphase Flow: From Laboratory Measurements to Field Applications*. 2012 by American Chemical Society. USA

Stackelberg, M.; Muller, H. R. *Z. Electrochemie* **1954**, *58*, 25

Stackelberg, M. *Recueil* **1956**, *75*, 902

Svandal, A., Kvamme, B., Granasy, L., Pusztai, T., *J. Phase Equilib. Diffusion*, **26**, 534, (2005).

Svartås Thor Martin, Pictures. 2013

Svartås T.M., Aas B., Fjelde I., *Hydrate Inhibition*. 2002 by Rogaland Research, RF. Stavanger

Svartås T.M. *Studies of novel hydrate inhibitors*. 1994. Stavanger

Taylor, C.J., Dieker, L.D., Miller, K.T., Koh, C.A., Sloan, E.D., *J. Colloid Interface Sci.*, (2006).

Topham, D.R., *Chem. Eng. Sci.*, **39**, 821, (1984).

Uchida, T., Ebinuma, T., Kawabata, J., Narita, H., *J. Cryst. Growth*, **204**, 348 (1999a).

Uchida, T., Ebinuma, T., Mae, S., *Formation Rate Measurements of CO_2 Hydrate Film Formed at Liquid CO_2 Water Interface, Greenhouse Gas Control Technologies*, Riemer, P., Eliasson, B.,Wokaun, A., eds. Elsevier, 1073, (1999).

Uchida, T., Ikeda, I.Y., Takeya, S., Ebinuma, T., Nagao, J., Narita, H., *J. Cryst. Growth*, **237–239**, 383 (2002).

Wyslouzil, B. E.; Cheung, J. L.; Wilemski, G.; Strey, R. *Phys. Rev. Lett.* **1997**, *79*.

www.fluidat.com

Zatsepina, O.Y. and B.A. Buffett, *Nucleation of CO2-hydrate in a porous medium*. Fluid Phase Equilibria, 2002.

Zerpa Luis E., Sloan E. Dendy, Sum Amadeu K., Koh Carolyn A., *Overview of CSMHyK: A transient hydrate formation model*. 2012 by Elsevier B.V. USA

Appendix

APPENDIX A: Gas consumption analysis:

Small cell:

Experiments	Gas flow top	Sum AUC
8 °C		
50 ml 500 RPM 1	134,8	2478,6
50 ml 500 RPM 2	151,4	3755,6
50 ml 500 RPM 3	139,4	2340,3
100 ml 500 RPM 1	102,1	3625,0
100 ml 500 RPM 2	97,8	3295,8
100 ml 500 RPM 3	94,2	3902,8
50 ml 700 RPM 1	252,3	2759,4
50 ml 700 RPM 2	279,8	2416,8
50 ml 700 RPM 3	241,1	2942,4
100 ml 700 RPM 1	192,3	3068,3
100 ml 700 RPM 2	193,8	3074,7
100 ml 700 RPM 3	205,1	3402,8
50 ml 1200 RPM 1	323,1	3745,4
50 ml 1200 RPM 2	314,5	1927,5
50 ml 1200 RPM 3	329,8	2030,4
100 ml 1200 RPM 1	446,0	3981,2
100 ml 1200 RPM 2	376,7	3995,6
100 ml 1200 RPM 3	400,6	3942,4
7 °C		
50 ml 500 RPM 1	174,5	2462,7
50 ml 500 RPM 2	181,6	2716,4
50 ml 500 RPM 3	192,5	3253,0
100 ml 500 RPM 1	176,2	4617,3
100 ml 500 RPM 2	153,5	3815,2
100 ml 500 RPM 3	143,9	3570,9
100 ml 500 RPM 4	141,6	3813,0
50 ml 700 RPM 1	469,4	3079,1
50 ml 700 RPM 2	360,4	3615,0
50 ml 700 RPM 3	375,6	3080,7
100 ml 700 RPM 1	226,6	3152,4
100 ml 700 RPM 2	209,4	3210,1
100 ml 700 RPM 3	259,4	3058,5
50 ml 1200 RPM 1	520,9	2884,3
50 ml 1200 RPM 2	528,0	2985,7
50 ml 1200 RPM 3	393,3	1601,7
50 ml 1200 RPM 4	591,8	3318,5
100 ml 1200 RPM 1	579,7	3875,1
100 ml 1200 RPM 2	784,6	3933,9
100 ml 1200 RPM 3	507,0	3718,7

6 °C		
50 ml 500 RPM 1	262,4	2099,2
50 ml 500 RPM 2	245,2	2430,0
50 ml 500 RPM 3	234,9	2292,1
100 ml 500 RPM 1	155,7	4345,0
100 ml 500 RPM 2	259,5	3842,3
100 ml 500 RPM 3	199,3	4304,1
50 ml 700 RPM 1	412,3	4439,5
50 ml 700 RPM 2	412,6	2333,7
50 ml 700 RPM 3	401,1	1857,9
100 ml 700 RPM 1	262,8	3458,1
100 ml 700 RPM 2	273,4	3218,5
100 ml 700 RPM 3	249,3	3156,1
50 ml 1200 RPM 1	560,1	3030,6
50 ml 1200 RPM 2	600,3	3340,9
50 ml 1200 RPM 3	666,8	6255,7
50 ml 1200 RPM 4	562,6	2824,6
100 ml 1200 RPM 1	667,1	3776,1
100 ml 1200 RPM 2	718,6	3731,6
100 ml 1200 RPM 3	702,6	3816,0

Big cell:

Experiments	Gas flow top	Sum AUC
8 °C		
112.5 ml 700 RPM 1	368,0	10132,9
112.5 ml 700 RPM 2	367,9	8979,7
112.5 ml 700 RPM 3	459,7	7580,2
225 ml 700 RPM 1	376,9	4447,6
225 ml 700 RPM 2	353,1	4466,9
225 ml 700 RPM 3	403,8	4262,9

Average results from the gas consumption analysis small cell

Experiments	Gas flow top	Sum AUC
8 °C		
50 ml 500 RPM	141.9	2858.1
100 ml 500 RPM	98.0	3607.9
50 ml 700 RPM	257.7	2706.2
100 ml 700 RPM	197.1	3181.9
50 ml 1200 RPM	322.4	2567.7
100 ml 1200 RPM	407.8	3973.1
7 °C		
50 ml 500 RPM	182.9	2810.7
100 ml 500 RPM	153.8	3954.1
50 ml 700 RPM	401.8	3258.3
100 ml 700 RPM	231.8	3140.3
50 ml 1200 RPM	508.5	2697.6
100 ml 1200 RPM	623.8	3842.6
6 °C		
50 ml 500 RPM	247.5	2273.7
100 ml 500 RPM	204.833333	4163.8
50 ml 700 RPM	408.7	2877.0
100 ml 700 RPM	261.9	3277.6
50 ml 1200 RPM	597.5	3863.0
100 ml 1200 RPM	696.1	3774.6

Table 4.2: Average results from the gas consumption analysis large cell

Experiments	Gas flow top	Sum AUC
8 °C		
112.5 ml 700 RPM	398.5	8897.6
225 ml 700 RPM	377.9	4392.5

APPENDIX B: Linear growth rate analysis:

Experiment	Initial rate (1)	Mid-section (2)	End-section (3)
8 °C			
100 ml 1200 RPM			
1	202,3	98,9	38,1
2	205,2	119,9	62,1
3	201,0	99,5	53,7
Average	202,8	106,1	51,3
50 ml 1200 RPM			
1	245,8	51,2	66,3
2	235,5	48,9	59,5
3	226,4	50,8	66,6
Average	235,9	50,3	64,1
100 ml 700 RPM			
1	160,2	97,4	50,8
2	161,7	96,0	51,0
3	175,6	99,0	53,1
Average	165,8	97,5	51,6
50 ml 700 RPM			
1	230,9	38,9	57,0
2	259,6	51,7	62,3
3	232,0	51,9	73,1
Average	240,9	47,5	64,1
100 ml 500 RPM			
1	85,3	47,9	40,5
2	89,0	53,2	46,4
3	78,1	58,2	38,3
Average	84,1	53,1	41,8
50 ml 500 RPM			
1	131,9	74,7	85,3
2	141,3	74,6	101,6
3	129,9	68,8	87,9
Average	134,4	72,7	91,6
7 °C			
100 ml 1200 RPM			
1	286,2	138,9	68,2
2	294,5	149,5	67,0
3	276,8	143,8	68,1
Average	285,8	144,1	67,8
50 ml 1200 RPM			
1	355,9	58,5	75,4
2	340,6	70,3	85,4
3	261,4	53,2	61,5
4	355,9	61,8	71,6
Average	328,4	61,0	73,5
100 ml 700 RPM			
1	171,9	108,8	58,0

2	141,0	155,3	76,7
3	197,1	112,1	63,9
Average	170,0	125,4	66,2
50 ml 700 RPM			
1	387,5	63,7	74,0
2	243,8	54,5	70,8
3	311,6	48,0	64,0
Average	314,3	55,4	69,6
100 ml 500 RPM			
1	64,8	59,6	70,2
2	100,8	83,0	63,6
3	101,5	79,9	61,1
4	78,2	91,4	63,2
Average	86,3	78,5	64,5
50 ml 500 RPM			
1	165,4	69,0	88,6
2	168,7	77,9	76,0
3	159,4	74,6	124,6
Average	164,5	73,8	96,4
6 °C			
100 ml 1200 RPM			
1	351,8	178,8	74,3
2	349,1	171,6	72,3
3	337,8	180,2	75,0
Average	346,2	176,8	73,8
50 ml 1200 RPM			
1	392,5	67,3	98,7
2	422,8	70,8	93,1
3	559,0	135,8	159,2
4	419,7	70,1	85,0
Average	448,5	86,0	109,0
100 ml 700 RPM			
1	220,9	140,4	80,8
2	225,1	158,2	79,8
3	224,7	148,9	76,0
Average	223,6	149,2	78,9
50 ml 700 RPM			
1	318,2	80,7	80,4
2	319,7	84,2	85,5
3	310,5	84,4	80,6
Average	316,1	83,1	82,2
100 ml 500 RPM			
1	102,7	180,2	83,0
2	101,2	172,0	89,1
3	134,1	137,4	87,4
Average	112,7	163,2	86,5
50 ml 500 RPM			
1	205,0	102,1	117,0

2	194,8	94,8	106,6
3	188,1	83,3	113,7
Average	196,0	93,4	112,4

Average results from the linear analysis from the small cell

Experiments	Initial-section (1) [ml/min]	Mid-section (2) [ml/min]	End-section (3) [ml/min]
8 °C			
100 ml 1200 RPM	202.83	106.089	51.335
50 ml 1200 RPM	235.873	50.270	64.121
100 ml 700 RPM	165.82	97.471	51.62
50 ml 700 RPM	240.85	47.48	64.14
100 ml 500 RPM	84.14	53.08	41.76
50 ml 500 RPM	134.36	72.71	91.60
7 °C			
100 ml 1200 RPM	285.81	144.06	67.75
50 ml 1200 RPM	328.43	60.974	73.489
100 ml 700 RPM	170	125.38	66.19
50 ml 700 RPM	314.31	55.43	69.62
100 ml 500 RPM	86.339	78.475	64.527
50 ml 500 RPM	164.50	73.83	96.42
6 °C			
100 ml 1200 RPM	346.22	176.83	73.84
50 ml 1200 RPM	==411.68==	==69.391==	==92.289==
100 ml 700 RPM	223.56	149.16	78.90
50 ml 700 RPM	316.13	83.13	82.16
100 ml 500 RPM	112.67	163.17	86.51
50 ml 500 RPM	195.98	93.42	112.41

Average results from the linear analysis from the large cell

Experiments	Initial-section (1) [ml/min]	Mid-section (2) [ml/min]	End-section (3) [ml/min]
8 °C			
225 ml 700 RPM	263.2033	199.1067	202.4067
112.5 ml 700 RPM	279.59	85.925	103.3807

APPENDIX C: Water left in the cell:

Small cell:

Experiment	Water converted [%]
8 °C	
50 ml 500 RPM 1	76.86
50 ml 500 RPM 2	75.10
50 ml 500 RPM 3	76.98
100 ml 500 RPM 1	85.25
100 ml 500 RPM 2	84.10
100 ml 500 RPM 3	85.47
50 ml 700 RPM 1	81.87
50 ml 700 RPM 2	76.72
50 ml 700 RPM 3	75.54
100 ml 700 RPM 1	85.39
100 ml 700 RPM 2	85.28
100 ml 700 RPM 3	84.70
50 ml 1200 RPM 1	80.90
50 ml 1200 RPM 2	81.73
50 ml 1200 RPM 3	81.48
100 ml 1200 RPM 1	82.08
100 ml 1200 RPM 2	80.75
100 ml 1200 RPM 3	82.47
7 °C	
50 ml 500 RPM 1	76.33
50 ml 500 RPM 2	76.99
50 ml 500 RPM 3	72.06
100 ml 500 RPM 1	84.52
100 ml 500 RPM 2	82.25
100 ml 500 RPM 3	82.81
100 ml 500 RPM 4	83.28
50 ml 700 RPM 1	70.37
50 ml 700 RPM 2	73.32
50 ml 700 RPM 3	75.83
100 ml 700 RPM 1	86.43
100 ml 700 RPM 2	84.55
100 ml 700 RPM 3	85.35
50 ml 1200 RPM 1	80.85
50 ml 1200 RPM 2	78.69
50 ml 1200 RPM 3	84.61
50 ml 1200 RPM 4	80.92
100 ml 1200 RPM 1	86.43
100 ml 1200 RPM 2	84.55
100 ml 1200 RPM 3	85.35
6 °C	
50 ml 500 RPM 1	79.82
50 ml 500 RPM 2	80.32
50 ml 500 RPM 3	81.40

100 ml 500 RPM 1	82.04
100 ml 500 RPM 2	81.51
100 ml 500 RPM 3	81.47
50 ml 700 RPM 1	82.38
50 ml 700 RPM 2	81.58
50 ml 700 RPM 3	82.15
100 ml 700 RPM 1	85.25
100 ml 700 RPM 2	84.52
100 ml 700 RPM 3	85.18
50 ml 1200 RPM 1	71.68
50 ml 1200 RPM 2	72.10
50 ml 1200 RPM 3	51.76
50 ml 1200 RPM 4	72.84
100 ml 1200 RPM 1	82.10
100 ml 1200 RPM 2	82.04
100 ml 1200 RPM 3	81.98

Big cell:

Experiments	Water converted
8 °C	
112.5 ml 700 RPM 1	67.66
112.5 ml 700 RPM 2	67.75
112.5 ml 700 RPM 3	67.56
225 ml 700 RPM 1	92.47
225 ml 700 RPM 2	90.88
225 ml 700 RPM 3	90.90

APPENDIX D: Simulation results, the heat of reaction results

Small cell

	Min [J/mol]	Max [J/mol]	Average [J/mol]
6 ℃ 50 ml 500 RPM			
1	-823627,4	2296920,2	83677,0
2	11543,2	1533063,0	72681,4
3	15553,0	1403725,3	66363,8
6 ℃ 50 ml 700 RPM			
1	-15861,6	231544,7	76288,1
2	1724,2	123431,2	73271,0
3	11489,6	409737,3	68747,5
6 ℃ 50 ml 1200 RPM			
1	-1563,4	174002,7	67676,9
2	-1118091,4	189351,2	75071,1
~~3~~	~~703,3~~	~~123886,3~~	~~44664,6~~
4	-20372,9	306780,7	67206,2
6 ℃ 100 ml 500 RPM			
1	-134801,8	1899559,1	58965,3
2	-29631,6	2374733,0	57140,3
3	-399569,2	488378,1	47990,8
6 ℃ 100 ml 700 RPM			
1	-43975,4	750581,3	59000,1
2	-30186,1	1605218,0	60025,8
3	-36482,2	662913,4	61958,4
6 ℃ 100 ml 1200 RPM			
1	-103578,5	449821,4	62707,8
2	-121708,8	766491,8	64886,4
3	-107864,5	628739,1	62077,7
7 ℃ 50 ml 500 RPM			
1	12657,9	1552545,1	57366,9
2	7124,1	2474432,9	77947,6
3	15873,9	2154866,6	76251,0
7 ℃ 50 ml 700 RPM			
1	8753,0	1272240,4	84891,6
2	17237,3	1115298,4	79191,7
3	8833,1	1351779,4	83608,8
7 ℃ 50 ml 1200 RPM			
1	-3777,8	250571,2	58348,5
2	-29580,0	257912,4	67009,5
3	-25737,7	989394,5	68984,2
4	-10736,3	124898,0	66399,0
7 ℃ 100 ml 500			

RPM			
1	-110880,4	2728535,5	59438,6
2	-49819,0	2358510,5	64135,8
3	-50869,8	2792162,6	63385,1
4	-76462,5	3183039,6	61787,8
7 °C 100 ml 700 RPM			
1	-27262,7	2057789,3	54851,0
2	-13903,4	1327735,4	43790,8
3	-18332,4	1541938,0	62290,4
7 °C 100 ml 1200 RPM			
1	-256058,7	611216,4	58818,5
2	-59786,8	359702,4	52855,3
3	-96087,6	398992,0	50858,0
8 °C 50 ml 500 RPM			
1	16779,9	2828171,4	75423,5
2	10497,4	2892990,4	69132,3
3	14530,4	2273544,1	69295,9
8 °C 50 ml 700 RPM			
1	1881,5	372813,9	52514,9
2	13673,7	128104,0	46084,3
3	18873,7	1209610,7	70215,9
8 °C 50 ml 1200 RPM			
1	-10826,1	494122,7	70315,9
2	-6711619,3	3484418,4	56825,1
3	-11046,9	135628,5	62551,1
8 °C 100 ml 500 RPM			
1	-68167,9	2320128,5	61071,7
2	-32686,3	2096815,8	58225,3
3	-2585285,2	2601355,3	62309,4
8 °C 100 ml 700 RPM			
1	-42827,1	1566993,4	51020,1
2	-34941,6	1847380,4	48944,6
3	-18629,9	768307,7	53267,2
8 °C 100 ml 1200 RPM			
1	-156219,1	920326,9	26047,2
2	-182069,0	743914,2	24939,8
3	-60482,2	3672515,1	37624,8

Big cell

	Min [J/mol]	Max [J/mol]	Average [J/mol]
8 ℃ 112.5 ml 700 RPM			
1	-551392,8	530939,0	101335,6
2	-603451,9	877790,1	97757,5
3	-63711,4	2775449,6	109302,2
8 ℃ 225 ml 700 RPM			
1	-92505,2	2412408,1	61762,0
2	-4407840,3	1674906,1	22698,3
3	-659160,7	304554,8	29087,4

APPENDIX E: The simulation program

```
%%%%%%%%%%%%%%%%%%%%%%%%%%%%%%%%%%%%%%%%%%%%%%%%%%%%%%%%%%%%%%%%%%%%
% Simulating radial heat transfer through titanium hydrate cell using the
% implicit discretization scheme.
% NB! In order to run, the outer border temperature vector TO must be
% imported to the workspace first; in order to compare with measured
% results, the representative interior temperature TIr is also needed.
% (and to initialize properly)
%
% Modified 22.04.2013 to include hydrate generation; values for hI and hO
% are obtained by tuning from tests w/o hydrate.
%
% Modofied 24-05 to take into account that the gas content is varying. The
% current gas content in moles must be imported in a vector called Ng


% Constants:
% Titanuim:
k   = 21.9;  % W/m K
rho = 4506;  % kg/m3
c   = 544;   % J/kg K
% Cylinder:
Ri      = 0.045;  % m
Ro      = 0.060; % m
delta   = 0.05;  % m
% Fluids:
mw      = 0.1125; % kg
cw      = 4200; % J/kg K
% Cancel Ng for time varying gas content
% Ng      = 0.426;  % mole
Cpg     = 49;   % J/mole K
% Heat transfer coefficients:
hI      = 200;  % W/m2 K
hO      = 2600;  % W/m2 K
% Grid:
N   = 18;
Dt  = 3;     % s
% Calculated properties:
alpha   = k/(rho*c);
Dr      = (Ro - Ri)/N;
Fo      = alpha*Dt/Dr^2;
BiI     = hI*Dr/k;
BiO     = hO*Dr/k;
% CI needs recalculation for each time step in case of time varying gas
% content (This value is initial value)
% CI      = 2*hI*pi*delta*Ri*Dt/(mw*cw + Ng*Cpg)
CI      = 2*hI*pi*delta*Ri*Dt/(mw*cw + Ng(1,1)*Cpg);
% Time steps in current border vector:
s       = size(TO);
s(:,2)  = [];
M   = s
% R-vector for plotting (R = 0 for interior of cell)
%R       = [];
%R(1,1)  = 0;
%for i   = 2:(N+2)
%    R(i,1)   = Ri + (i-2)*Dr;
%end



%Setting up the A-matrix for hydrate generation
```

```matlab
%(This is ALMOST constant throughout, so this is an initialization):
A    = [];
% First row; entry I - cell interior:
A(1,1)  = 1;
A(1,2)  = CI;
for j    = 3:(N+2)
    A(1,j)  = 0;
end
% Second row; entry 0 - inner border/wall:
A(2,1)  = 0;
A(2,2)  = (1 + 2*(BiI + (Dr/(2*Ri) + 1))*Fo);
A(2,3)  = -2*(Dr/(2*Ri) + 1)*Fo;
for j    = 4:(N+2)
    A(2,j)  = 0;
end
% Internal node rows 1 - (n-1) => i = 3 - (N+1):
for i    = 3:(N+1)
    for j    = 1:(i-2)
        A(i,j)  = 0;
    end
    r    = Ri + (i-2)*Dr;
    A(i,(i-1))  = (Dr/(2*r) - 1)*Fo;
    A(i,i)      = (1 + 2*Fo);
    A(i,(i+1))  = -(Dr/(2*r) + 1)*Fo;
    for j    = (i+2):(N+1)
        A(i,j)  = 0;
    end
end
% Last row; entry N+2 - outer border:
for j    = 1:N
    A((N+2),j)  = 0;
end
A((N+2),(N+1))  = 2*(Dr/(2*Ro) - 1)*Fo;
A((N+2),(N+2))  = (1 + 2*(BiO - (Dr/(2*Ro) - 1))*Fo);
%Inverting the A-matrix: (This must be moved inside the loop in case of
%time varyig gas content)
% AI  = inv(A);


% Initializing the Y-vector:
Y    = [];
% Cell internal:
Y(1,1)  = (1 + CI)*TIr(2,1) - TIr(1,1);
% Inner wall:
Y(2,1)  = TIr(1,1) + 2*BiI*Fo*TIr(2,1);
for i    = 3:9
    Y(i,1)  = TIr(1,1);
end
for i    = 10:(N+1)
    Y(i,1)  = TO(1,1);
end
Y((N+2), 1) = TO(1,1) + 2*BiO*Fo*TO(2,1);
%Y
%pause;
% Vectors for time series plotting:
Time    = [];
TI      = [];   % Interior; i.e. the temperature of the fluids (g + w)
TOp     = [];   % Need an extra plotting vector for the bath temperature
                %(to be of the same length as the time vector)
TWI     = [];   % Need to plot the wall temperatures too, sometimes
TWO     = [];   % TWI = inner wall, TWO = outer wall
XI      = [];   % Group posing as temperature, from which the heat of
```

```matlab
                    % hydrate generation is to be derived from

% Starting time loop (With measured values the number of repetitions is
% given by the size of the input vecors, M):
t    = 0;
Time    = [Time; t];
TIp     = [TI; TIr(1,1)];
TOp     = [TOp; TO(1,1)];
TWI     = [TWI; TIr(1,1)]; % Estimat
TWO     = [TWO; TO(1,1)]; % Estimat
XI      = [XI; 0]; % Ingen varme generert ennå


for i   = 1:(M-2)
    % Inverting matrix:
    AI  = inv(A);
    % Calculate T-vector
    T   = AI*Y;
    % Filling vectors for plotting
    XI  = [XI; T(1,1)];
    TWI  = [TWI; T(2,1)];
    TWO  = [TWO; T((N+2),1)];
    TIp = [TIp; TIr((i+1),1)];
    TOp = [TOp; TO((i+1),1)];
    % Updating Y-vector
    Y    = T;
    CI          = 2*hI*pi*delta*Ri*Dt/(mw*cw + Ng((i+1),1)*Cpg);
    Y(1,1)      = (1 + CI)*TIr((i+2),1) - TIr((i+1),1);
    Y(2,1)      = T(2,1) + 2*BiI*Fo*TIr((i+2),1);
    Y((N+2), 1) = T((N+2),1) + 2*BiO*Fo*TO((i+2),1);
    % Updating A- matrix:
    A(1,2)      = CI;
    %Y
    %pause;
    t    = t + Dt;
    Time    = [Time; t];
end
t

% Plotting resulting time series to screen

figure(1);
plot(Time, XI);
%plot(R, T);
%axis([0, 0.045, 14, 18.5]);

figure(2);
plot(Time, TOp, 'r');
hold;
plot(Time, TIp, 'g');
plot(Time, TWI, 'y');
plot(Time, TWO);
hold;
```